

## Classification of solutions of the forced periodic nonlinear Schrödinger equation

This article has been downloaded from IOPscience. Please scroll down to see the full text article.

2010 Nonlinearity 23 2183

(<http://iopscience.iop.org/0951-7715/23/9/008>)

View [the table of contents for this issue](#), or go to the [journal homepage](#) for more

Download details:

IP Address: 132.77.4.43

The article was downloaded on 31/08/2010 at 12:52

Please note that [terms and conditions apply](#).

# Classification of solutions of the forced periodic nonlinear Schrödinger equation

Eli Shlizerman<sup>1</sup> and Vered Rom-Kedar<sup>2</sup>

Faculty of Mathematics and Computer Science, The Weizmann Institute of Science, Rehovot, 76100, Israel

<sup>1</sup>From 1 Sep 2009 affiliated with the Department of Applied Mathematics, University of Washington, Seattle, WA 98195, USA

<sup>2</sup>The Estrin family chair of Computer Science and Applied Mathematics

E-mail: [eli.shlizerman@weizmann.ac.il](mailto:eli.shlizerman@weizmann.ac.il) and [vered.rom-kedar@weizmann.ac.il](mailto:vered.rom-kedar@weizmann.ac.il)

Received 14 July 2009, in final form 30 April 2010

Published 10 August 2010

Online at [stacks.iop.org/Non/23/2183](http://stacks.iop.org/Non/23/2183)

Recommended by D V Treschev

## Abstract

The integrable structure of the periodic one-dimensional nonlinear Schrödinger equation is utilized to gain insights regarding the perturbed near-integrable dynamics. After recalling the known results regarding the structure and stability of the unperturbed standing and travelling waves solutions, two new stability results are presented: (1) it is shown numerically that the stability of the ‘outer’ (cnoidal) unperturbed solutions depends on their power (the  $L_2$  norm): they undergo a finite sequence of Hamiltonian–Hopf bifurcations as their power is increased. (2) another proof that the ‘inner’ (dnoidal) unperturbed solutions with multiplicity  $\geq 2$  are linearly unstable is presented. Then, to study the global phase-space structure, an energy–momentum bifurcation diagram (PDE-EMBD) that consists of projections of the unperturbed standing and travelling waves solutions to the energy–power plane and includes information regarding their linear stability is constructed. The PDE-EMBD helps us to classify the behaviour near the plane wave solutions: the diagram demonstrates that below some known threshold amplitude, precisely three distinct observable chaotic mechanisms arise: homoclinic chaos, homoclinic resonance and, for some parameter values, parabolic-resonance. Moreover, it appears that the dynamics of the PDE chaotic solutions that exhibit the parabolic-resonance instability may be qualitatively predicted: these exhibit the same dynamics as a recently derived parabolic-resonance low-dimensional normal form. In particular, these solutions undergo adiabatic chaos: they follow the level lines of an adiabatic invariant till they reach the separatrix set at which the adiabatic invariant undergoes essentially random jumps.

Mathematics Subject Classification: 35Q55, 70H11, 37Kxx

(Some figures in this article are in colour only in the electronic version)

## 1. Introduction

The one-dimensional nonlinear Schrödinger (NLS) equation is an integrable partial differential equation possessing an infinite number of symmetries corresponding to infinite number of conserved quantities. Indeed, utilizing the inverse scattering theory the one-dimensional NLS [1, 17, 42, 45] (on the line  $\mathbb{R}$  or the circle  $\mathbb{T}^1$ ) is solvable as an initial value problem. In the physical context, the NLS equation is a first order nonlinear model for the propagation of dispersive waves that interact nonlinearly and thus arises in various applications such as propagation of laser beams in optical fibres, surface waves and Bose–Einstein condensates. The role of the nonlinear terms has become especially significant in recent years, as high intensity laser beams [45] and Bose–Einstein condensates are realized experimentally [21]. The common nonlinearity for the NLS equation is the cubic nonlinearity and the sign of the nonlinearity (sign ( $g$ ) in equation (1.1)) determines its nature<sup>3</sup>: a defocusing equation for  $g < 0$  and a focusing equation for  $g > 0$ :

$$i\varphi_t - \varphi_{xx} - g|\varphi|^2\varphi = 0. \quad (1.1)$$

From the variety of solutions of the integrable one-dimensional NLS equation the solutions that attracted much attention of analytical, numerical and experimental studies are the standing waves or their generalization—the travelling waves (on  $\mathbb{R}$ , the famous solitary waves solutions correspond to the subclass of such waves having a finite ‘power’, namely a finite  $L_2$  norm) [3, 45]. The standing waves are solutions that are stationary in the spatial domain and periodic in time. The travelling waves have a fixed spatial profile that periodically oscillates in time and moves with a constant velocity in the spatial domain. The existence of stable standing/travelling waves is of high practical importance, for example for encoding and transmitting data in optical fibres [2, 44].

The linearization of the NLS equation about a standing wave solution boils down to solving the eigenvalue problem of a matrix operator  $N$  (see [55] and section 2.2). Although the linearized operator consists of two self-adjoint operators  $\mathcal{L}_+$  and  $\mathcal{L}_-$ , it is not self-adjoint and determining its eigenvalues is not a straightforward task. The linearized problem near the quiescent and the plane wave solutions is explicitly solvable by modulation stability analysis. In particular, as the amplitude of the plane wave grows, more modes become unstable, and the number of linearly unstable modes (LUMs) for a given plane wave amplitude may be explicitly computed (see [17] and section 2.2). The ground state standing waves on  $\mathbb{R}^N$  were proved to be nonlinearly stable by utilizing the framework developed by [9, 16] for the KdV equation and by [57] for the NLS equation. To deal with the other standing waves, a theoretical framework for proving linear instability was developed in [28–30, 36]. In this framework one deduces instability when the number of positive eigenvalues of the operator  $\mathcal{L}_+$  exceeds the number of positive eigenvalues of the operator  $\mathcal{L}_-$  by more than one (see section 2.2). Recently, these theories were applied to the one-pulse and two-pulse dnoidal standing waves of the one-dimensional NLS with periodic boundary conditions [6] and extended to provide counting of the number of unstable eigenvalues [33].

Here we consider this latter case of the focusing cubic one-dimensional NLS equation with periodic boundary conditions. The infinite-dimensional phase space is composed of level sets of the constants of motion. A level set corresponds generically to one or several infinite-dimensional tori. A solution of the NLS equation belonging to a generic regular level set is a quasi-periodic solution winding on a torus and can be decomposed into infinite set of action-angle coordinates. Each action-angle pair (a degree of freedom) can be considered as

<sup>3</sup> We keep the parameter  $g$ , which may be scaled out, to ease the comparison with previous works on the focusing equation in which  $g$  is taken to be either 1 or 2.

an oscillator and corresponds to an invariant of the integrable equation. The non-generic singular level sets may be composed of finite-dimensional tori (these may be viewed as degenerate infinite-dimensional tori) and possibly their stable and unstable manifolds (the linearized operator at the degenerate tori determines their linear stability). An example for such a singular level set is the one corresponding to standing/travelling wave solutions: then the degenerate torus is a circle. Indeed, standing and travelling waves were shown to exist in the focusing cubic NLS with periodic boundary conditions. In fact, these solutions can be found analytically, since they correspond to periodic solutions of the Duffing equation (see [6, 55] and section 2.1). These solutions become unstable as their amplitude increases and additional standing/travelling waves bifurcate from them (see [6, 24, 25, 33] and section 2.2). Note that due to integrability, even in the unstable cases, the solutions near the unstable waves are regular, namely quasi-periodic (see section 2.3).

In applications, the one-dimensional NLS appears only as a leading order approximation, and thus it is natural to consider the effect of small correction terms and forcing. The inclusion of such terms typically breaks the integrable structure [14]. If the forcing and correction terms are small, one may hope to be able to analyse the near-integrable PDE by perturbative methods. To study such systems, it was proposed to consider the simplest possible prototypical perturbations—spatially independent time-periodic forcing and damping [15, 17]:

$$i\varphi_t - \varphi_{xx} - g|\varphi|^2\varphi = \varepsilon \exp(-i\Omega^2 t + i\alpha) - i\delta\varphi, \quad \varphi_0(x) = \varphi(x, 0). \quad (1.2)$$

Here  $\varepsilon$  is the small forcing amplitude,  $\delta$  is the small damping coefficient (so, hereafter,  $\varepsilon, \delta \ll 1$ ),  $\Omega^2$  is the forcing frequency and  $\alpha$  is an arbitrary phase. Following [55], it is easy to show that for all  $\varphi_0 \in \mathcal{H}^1(\mathbb{T})$  there exist a unique  $\varphi \in C([0, \infty), \mathcal{H}^1(\mathbb{T}))$  that solves the initial value problem of equation (1.2).

A natural question that arises is how to characterize the solutions of the perturbed equation. Obtaining a complete infinite-dimensional phase space description of a non-integrable PDE which is not strongly dissipative appears to be too difficult. Traditionally, the structure of the phase space had been interpreted only near special solutions, usually only near the quiescent solution. For the near-integrable NLS equation, utilizing the known integrable phase-space structure near finite amplitude solutions such as standing/travelling waves, one may explore larger regions in the infinite-dimensional phase space. Indeed it was proposed that in the near-integrable setting, solutions with initial data near unstable standing wave solutions of the integrable equation may become irregular [13].

To gain intuition regarding the different mechanisms of irregularities in the near-integrable system when the plane wave has at most one LUM, a two-mode Galerkin truncation of the perturbed NLS was introduced [10–12, 17]. The unperturbed truncated system turned out to be a two degrees of freedom Hamiltonian system, with an additional integral of motion. These two integrals of motion were found to correspond to the first two invariants of the unperturbed PDE: the energy and the power (the  $L_2$  norm) of the solutions. As usual, most level sets of the two degree of freedom Hamiltonian correspond to one or two invariant two-tori. The spatial independent solutions of the NLS, the plane waves, appear as singular level sets, namely invariant circles of both the truncated and full PDE model. As their amplitudes increase these circles become normally unstable, and families of homoclinic orbits are created in both the ODE and the PDE models, leading to the creation of homoclinic chaos in the perturbed equation [23]. When the plane wave is both unstable and resonant, a novel mechanism of instability emerges—the hyperbolic resonance [31, 38]. New methodologies and tools introduced to this PDE–ODE study had finally led to a proof that the homoclinic resonance dynamics has analogous behaviour in the PDE setting [17, 32, 43]. To fully classify the near-integrable structure of the truncated model for all parameters  $k, \Omega$ , the hierarchy of bifurcations framework was developed [51].

The analysis showed that when the spatial box length and the frequency are close to the particular relation  $\Omega^2 = \Omega_{\text{pr}}^2 = k^2/2$  where  $k = 2\pi/L$ , the truncated NLS admits a new type of chaotic dynamics—parabolic resonant solutions (see [49] and section 3.3). In [52] it was demonstrated that analogous chaotic trajectories appear in the PDE setting.

Going beyond the two degrees of freedom regime, it was shown that in the dissipative case, when the resonant plane wave amplitude is increased so it has two or more LUMs, solutions with initial data near the plane wave evolve chaotically in both time and space so that their spatial coherence is lost—such solutions were called spatio-temporal chaotic (STC) [18]. Recently, we demonstrated that in the Hamiltonian case, the parabolic-resonance mechanism enables to drive solutions with small initial data (near the unperturbed stable plane wave) into STC with smaller forcing amplitude than the forcing amplitude needed to drive such data to STC in the elliptic or hyperbolic resonance cases [53].

In this paper, we propose that a specific bifurcation diagram, the PDE-EMBD is beneficial in studying how the infinite-dimensional integrable phase-space structure deforms when small perturbations are applied. The first part of the paper is devoted to constructing the diagram, namely studying the integrable structure (including some new results regarding the stability of some of the standing waves) whereas the second part is devoted to studying the near-integrable dynamics (including some new results regarding the parabolic-resonance mechanism). More specifically, in section 2 we review the relevant properties of the integrable periodic one-dimensional NLS, provide the analytic expressions for the standing and travelling waves solutions and study their stability. These results are then used for constructing the PDE-EMBD. In section 3 we employ this construction to analyse the dynamics near-plane waves of the near-integrable forced NLS. We review the known properties of such perturbed solutions and analyse the parabolic-resonance mechanism that was identified in the PDE in [52] and was described as a route from stability to spatio-temporal chaos in [53].

## 2. The unperturbed problem

### 2.1. Standing and travelling wave solutions

*2.1.1. General properties.* Consider the autonomous one-dimensional NLS equation with periodic boundary conditions (substituting in (1.2)  $\varphi = \psi \exp(-i\Omega^2 t + i\alpha)$ , and setting  $\varepsilon = \delta = 0$ ):

$$\begin{aligned} i\Psi_t &= \Psi_{xx} + (g|\Psi|^2 - \Omega^2)\Psi, \\ \Psi(x, 0) &= \Psi_0(x), \end{aligned} \quad (2.1)$$

where  $\Psi(x, t) = \Psi(x + L, t)$ ,  $x \in \mathbb{R}$ ,  $g = 2$  and  $\Psi_0(x) \in \mathcal{H}^r(\mathbb{T})$ ,  $r \geq 3$  (we will mostly consider the two-mode analytic initial data, see section 3) denotes the initial data profile. The NLS equation is integrable: it is completely solvable by the inverse scattering technique [42] and, for smooth initial data, it has an infinite number of constants of motion. The first three conserved quantities, ordered by the required number of spatial derivatives are

$$\text{Particle number : } I(\Psi) = \frac{1}{L} \int_{-L/2}^{L/2} |\Psi|^2 dx, \quad (2.2)$$

$$\text{Linear momentum : } P(\Psi) = \frac{1}{2iL} \int_{-L/2}^{L/2} \Psi \partial_x \Psi^* - \Psi^* \partial_x \Psi dx, \quad (2.3)$$

$$\text{Hamiltonian : } H_0(\Psi) = \frac{1}{L} \int_{-L/2}^{L/2} \left( -|\partial_x \Psi|^2 + \frac{g}{2} |\Psi|^4 - \Omega^2 |\Psi|^2 \right) dx. \quad (2.4)$$

These correspond to the conservation of mass, linear momentum and energy and can be easily shown to be invariants of the equation. Other conserved quantities involve higher spatial derivatives of the solution. The corresponding symmetries to equations (2.2)–(2.4) are phase translation, space translation and time translation (the *Galilean* transformation).

Thus if  $\Psi(x, t)$  is a solution of the NLS then so is the three-parameter family of solutions  $\Psi'(x, t; v, s, \theta)$ :

$$x' = x - vt + s, \tag{2.5}$$

$$\Psi'(x, t; v, s, \theta) = \Psi(x', t) \exp \left[ i \left( -\frac{v}{2}x + \frac{v^2}{4}t + \theta \right) \right]. \tag{2.6}$$

The same transformation applies to the periodic case, yet the periodic boundary conditions impose a quantization on the values of  $v$

$$v_j = \frac{4\pi}{L}j, \quad j \in \mathbb{Z},$$

whereas  $s, \theta$  remains arbitrary.

**2.1.2. Standing waves.** The standing waves are oscillatory in time separable solutions of the integrable NLS equation

$$\Psi_{sw}(x, t) = e^{-iE_\lambda t + iE_0 x} \Phi_{E_\lambda}(x), \tag{2.7}$$

where  $E_\lambda, \Phi_{E_\lambda}(x)$  are eigenvalues and eigenfunctions of the nonlinear operator  $\mathcal{N}$ :

$$\mathcal{N}(\Phi_{E_\lambda})\Phi_{E_\lambda} = (\partial_{xx} + g|\Phi_{E_\lambda}|^2 - \Omega^2)\Phi_{E_\lambda} = E_\lambda \Phi_{E_\lambda}, \tag{2.8}$$

$$\Phi_{E_\lambda}(x + L) = \Phi_{E_\lambda}(x). \tag{2.9}$$

Multiplying by  $\Phi_{E_\lambda}^*$  and integrating, the eigenvalue  $E_\lambda$  and the integral  $K$ , are defined by

$$E_\lambda = K(\Phi_{E_\lambda})/I(\Phi_{E_\lambda}), \tag{2.10}$$

$$K(\Psi) = \frac{1}{L} \int_{-L/2}^{L/2} (-|\partial_x \Psi|^2 + g|\Psi|^4 - \Omega^2|\Psi|^2) dx. \tag{2.11}$$

The linear momentum of the standing waves always vanishes,  $P(\Psi_{sw}) = 0$ . In general, the calculation of eigenvalues and eigenfunctions of nonlinear operators is a formidable task. However, for real  $\Phi_{E_\lambda}(x)$ , equation (2.8) corresponds to the Duffing equation:

$$\partial_{xx}\Phi_{E_\lambda} + g\Phi_{E_\lambda}^3 - (E_\lambda + \Omega^2)\Phi_{E_\lambda} = 0, \tag{2.12}$$

and its general solutions are explicitly given by Jacobi-elliptic functions (see [6] and below). Figure 1 shows the corresponding phase-portrait  $(\Phi_{E_\lambda}, \partial_x \Phi_{E_\lambda})$  of the Duffing equation for a fixed  $E_\lambda$ . There are different families of solutions: stable and unstable fixed points, homoclinic orbits<sup>4</sup>, solutions inside the homoclinic orbit—*inner solutions* and solutions outside of the homoclinic orbit—*outer solutions*. Next we show that imposing the periodic boundary conditions selects a discrete set of Duffing solutions that are either fixed points, periodic inner solutions or periodic outer solutions.

The quiescent fixed point (black),  $(\Phi_{E_\lambda}, \partial_x \Phi_{E_\lambda}) = (0, 0)$ , is a saddle (center) when  $E_\lambda > -\Omega^2$  (respectively when  $E_\lambda < -\Omega^2$ ). In the first case, the saddle has two homoclinic orbits that enclose the two stable fixed points (blue),  $(\Phi_{E_\lambda}, \partial_x \Phi_{E_\lambda}) = (\pm\sqrt{E_\lambda + \Omega^2}/g, 0)$ .

<sup>4</sup> these are the celebrated soliton solutions on the infinite line.

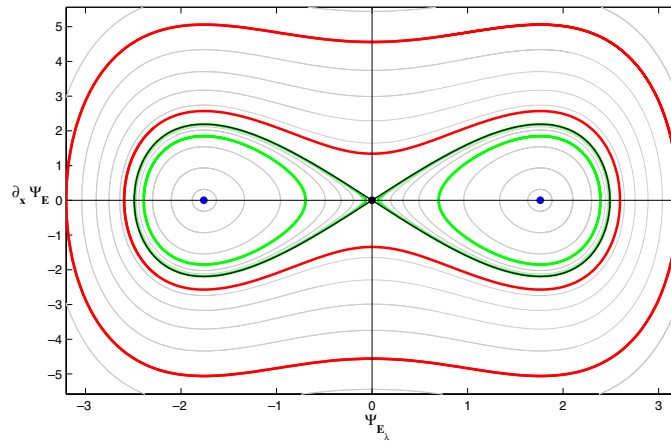


**Figure 1.** Phase space of the Duffing equation for  $g = 1, \Omega^2 = 1, L = 2\pi$  and  $E_\lambda = 3$ . The fixed points on the  $x$ -axis (blue) correspond to the NLS plane wave solutions  $(\pm\sqrt{(E_\lambda + \Omega^2)/g}, 0)$ . The NLS  $L$ -periodic inner solutions  $\Phi_j^{\text{int}}(x)$  and outer solutions  $\Phi_j^{\text{out}}(x)$  are marked in bold green and bold red, respectively.

These two centres correspond to the plane wave solutions of the NLS equation: they are spatially independent solutions, having a constant amplitude,  $\Phi_{E_\lambda}^{\text{pw}}(x) = |c|$ , and thus

$$\Psi_{\text{pw}}(x, t) = |c|e^{iy(t)} = |c|e^{-iE_\lambda^{\text{pw}}t + iE_0} \tag{2.13}$$

where from (2.2), (2.4) and (2.10) the phase velocity and the constants of motion of the plane wave are

$$E_\lambda^{\text{pw}}(|c|; g, \Omega^2) = -\Omega^2 + g|c|^2, \quad I^{\text{pw}} = |c|^2 = \frac{(E + \Omega^2)}{g}, \quad H_0^{\text{pw}} = \frac{g}{2}I^2 - \Omega^2I. \tag{2.14}$$

The general outer solutions of the Duffing equation are found in terms of the Jacobi-elliptic functions:

$$\begin{aligned} \Phi_{E_\lambda, \kappa}^{\text{out}}(x) &= a_2 \sqrt{\frac{2\kappa^2}{g}} \mathbf{cn}(a_2x, \kappa), & a_2 &= \frac{2\pi}{L} \sqrt{\frac{E_\lambda + \Omega^2}{2\kappa^2 - 1}}, \\ \partial_x \Phi_{E_\lambda, \kappa}^{\text{out}}(x) &= -a_2^2 \sqrt{\frac{2}{g}} \frac{\kappa^2 L}{2\pi} \mathbf{sn}(a_2x, \kappa) \mathbf{dn}(a_2x, \kappa), \end{aligned} \tag{2.15}$$

and their (spatial) period is

$$L^{\text{out}}(\kappa, E_\lambda + \Omega^2) = 4\sqrt{\frac{2\kappa^2 - 1}{E_\lambda + \Omega^2}} K(\kappa),$$

where  $K(\kappa)$  is the Jacobi complete elliptic integral of the first kind. Since the standing wave solutions must be  $L$ -periodic, the condition

$$L^{\text{out}}(\kappa, E_\lambda + \Omega^2) \Big|_{\kappa=\kappa_j} = \frac{L}{j}, \quad j \in \mathbb{N} \tag{2.16}$$

leads to a selection, for any given  $E_\lambda$ , of a finite number of values  $\kappa_j(E_\lambda)$  at which the spatial-period satisfies this ‘quantization’ rule, see bold (red) curves outside the homoclinic orbit in

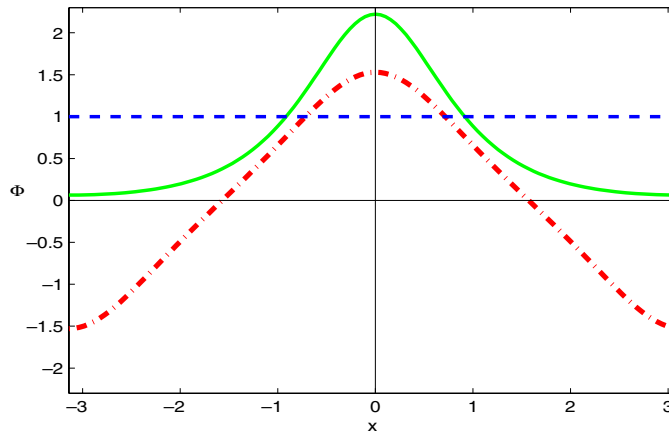


**Figure 2.** Three different types of standing waves profiles. Solutions of equation (2.12) at  $\Omega^2 = 1$ , with  $L^{\text{int, out}}(k, E_\lambda) = L$  and  $I(\Phi^{\text{pw, int, out}}) = 1$  are shown. The flat plane wave profile  $\Phi^{\text{pw}}(x)$  is marked by a dashed (blue) line. The standing wave profile  $\Phi_1^{\text{int}}(x)$  is marked by a solid (green) line and the profile  $\Phi_1^{\text{out}}(x)$  is marked by a dashed–dotted (red) line.

figure 1 and the dotted dashed (red) curve in figure 2. Since  $\partial L^{\text{out}}/\partial k \neq 0$  by the implicit function theorem the elliptic modulus  $\kappa_j(E_\lambda)$  is a function of the variable  $E_\lambda$  and can be found by solving the equation  $L^{\text{out}} = L/j$ .

For small  $\kappa$  and negative  $E_\lambda + \Omega^2$ ,  $\Phi_{E_\lambda, \kappa}^{\text{out}}(x)$  is well approximated by the solutions to the linearized equation near the quiescent solution:

$$\Phi_{E_\lambda, \kappa}^{\text{out}}(x) \xrightarrow{\kappa \rightarrow 0} \Phi_{E_\lambda}^{\text{lin}}(x) = \cos(\sqrt{-(E_\lambda + \Omega^2)}x + \theta), \quad (2.17)$$

where  $\Phi_{E_\lambda}^{\text{lin}}(x)$  solves the ‘linear standing wave’ equation

$$\partial_{xx} \Phi_{E_\lambda}^{\text{lin}} - (E_\lambda + \Omega^2) \Phi_{E_\lambda}^{\text{lin}} = 0. \quad (2.18)$$

These linear solutions are  $L$  (in fact  $L/j$ ) periodic when  $E_\lambda = E_{\lambda, j}^{\text{out}}$ :

$$E_{\lambda, j}^{\text{out}} = -\Omega^2 - \left(\frac{2\pi j}{L}\right)^2 \quad (2.19)$$

and the discrete set of outer  $j$  oscillatory solutions asymptotes to these linear solutions in the small amplitude limit:

$$\Phi_j^{\text{out}}(x; E_\lambda) := \Phi_{E_\lambda, \kappa_j(E_\lambda)}^{\text{out}}(x) \xrightarrow{\kappa_j \rightarrow 0, E_\lambda \rightarrow E_{\lambda, j}^{\text{out}}} \Phi_{E_{\lambda, j}^{\text{out}}}^{\text{lin}}(x). \quad (2.20)$$

Similarly, the inner  $L^{\text{int}}$  periodic solutions (bold (green) curves inside the homoclinic orbit in figure 1 and solid (green) curve in figure 2) are

$$\Phi_{E_\lambda, \kappa}^{\text{int}}(x) = a_1 \sqrt{\frac{2}{g}} \mathbf{dn}(a_1 x, \kappa), \quad a_1 = \frac{2\pi}{L} \sqrt{\frac{E_\lambda + \Omega^2}{(2 - \kappa^2)}}, \quad (2.21)$$

$$\partial_x \Phi_{E_\lambda, \kappa}^{\text{int}}(x) = -a_1^2 \sqrt{\frac{2}{g}} \frac{\kappa^2 L}{2\pi} \mathbf{sn}(a_1 x, \kappa) \mathbf{cn}(a_1 x, \kappa),$$

where  $\kappa = \kappa(E_\lambda)$  is the elliptic modulus of the solution, with period  $L^{\text{int}}(\kappa, E_\lambda + \Omega^2)$

$$L^{\text{int}}(\kappa, E_\lambda + \Omega^2) = 2\sqrt{\frac{2 - \kappa^2}{E_\lambda + \Omega^2}} K(\kappa). \quad (2.22)$$

As for the outer solutions, the elliptic modulus is determined by solving the equation  $L^{\text{int}} = L/j$ . As  $\kappa \rightarrow 0$ , the inner solutions  $\Phi_{E_\lambda, \kappa}^{\text{int}}(x)$  asymptote to the linear solution around the plane wave solution. Requiring  $L^{\text{int}}(\kappa_j(E_\lambda), E_\lambda + \Omega^2) = L/j$ , the  $j$ -pulse branches are defined as

$$\Phi_j^{\text{int}}(x; E_\lambda) := \Phi_{E_\lambda, \kappa_j(E_\lambda)}^{\text{int}}(x) \xrightarrow{\kappa_j \rightarrow 0, E_\lambda \rightarrow \tilde{E}_{\lambda, j}} \Phi_{\tilde{E}_{\lambda, j}}^{\text{pw}}(x) + \tilde{\Phi}_{\tilde{E}_{\lambda, j}}^{\text{lin}}(x), \tag{2.23}$$

where  $\tilde{\Phi}_{\tilde{E}_{\lambda, j}}^{\text{lin}}(x) = \Phi_{\tilde{E}_{\lambda, j}}^{\text{lin}}(x)$  so the  $L/j$  periodicity implies

$$\tilde{E}_{\lambda, j} = -\Omega^2 + \frac{1}{2} \left( \frac{2\pi j}{L} \right)^2. \tag{2.24}$$

Summarizing, there are two sets of families of  $L$  periodic  $j$ -oscillatory solutions: the outer families  $\Phi_j^{\text{out}}(x; E_\lambda)$  that have  $2j$  zeroes in a period, and the inner solutions,  $\Phi_j^{\text{int}}(x; E_\lambda)$  that do not change their sign (hereafter, when there is no ambiguity, we omit the explicit dependence of these solutions on  $E_\lambda$  and denote  $\Phi_j^{\text{int, out}}(x) = \Phi_j^{\text{int, out}}(x; \cdot)$ ).

*2.1.3. Travelling waves.* Applying the symmetry group transformation (equation (2.6)) to the standing waves solutions  $\Psi(x, t) = \Phi_{E_\lambda}(x)e^{-iE_\lambda t}$ , where  $\Phi_{E_\lambda}$  is either a plane wave, an interior or an exterior  $L$ -periodic solution) produces three-parameter families of travelling waves solutions where the parameter  $v$ , the speed of the travelling wave, is discrete, and  $s$  and  $\theta$ , its space and phase shifts, are continuous. To determine the corresponding eigenvalues of the travelling waves, we note that if one defines  $\Psi'(x, t; v_j, s, \theta) = \Phi'_{E'_\lambda}(x')e^{-iE'_\lambda t}$  where

$$E'_\lambda = E_\lambda - \frac{v_j^2}{4}. \tag{2.25}$$

then  $\Psi'$  satisfies equation (2.8) with  $x'$  and  $E'_\lambda$  replacing  $x$  and  $E_\lambda$ . Regarding the other constants of motion, the transformation preserves the  $L_2$ -norm

$$I(\Psi'(x, t; v_j, s)) = I(\Psi(x, t)) \tag{2.26}$$

yet changes the Hamiltonian

$$H_0(\Psi'(x, t; v_j, s)) = H_0(\Psi(x, t)) - \frac{v_j^2}{4} I(\Psi(x, t)), \tag{2.27}$$

and the linear momentum

$$P(\Psi'(x, t; v_j, s)) = -\frac{v_j}{2} I(\Psi(x, t)). \tag{2.28}$$

*2.2. Stability*

Linearization about the standing wave solutions leads to the equation

$$i\xi_t = \xi_{xx} - (E_\lambda + \Omega^2)\xi + g(2\Phi_{E_\lambda}^2(x)\xi + \Phi_{E_\lambda}^2(x)\xi^*), \tag{2.29}$$

where  $\xi$  is the perturbation and  $\xi^*$  denotes the complex conjugate of  $\xi$ . The dependence of  $\xi$  on time (oscillatory, exponentially increasing/decreasing) determines the linear stability of  $\Phi_{E_\lambda}$ . For a general standing wave solution, equation (2.29) can be rewritten as [30, 35, 36]

$$\begin{aligned} i(\xi - \xi^*)_t &= \mathcal{L}_+(\xi + \xi^*), \\ i(\xi + \xi^*)_t &= \mathcal{L}_-(\xi - \xi^*). \end{aligned} \tag{2.30}$$

The operators  $\mathcal{L}_+$  and  $\mathcal{L}_-$  are of Hill's type—these are second order differential operators with periodic potential and periodic boundary conditions

$$\begin{aligned} \mathcal{L}_+ : \quad & \mathcal{L}_+[x, \Phi_{E_\lambda}(x)]u = (\partial_{xx} - (E_\lambda + \Omega^2) + 3g\Phi_{E_\lambda}^2(x))u, \\ & u(-L/2) = u(L/2), \quad u'(-L/2) = u'(L/2), \end{aligned}$$

$$\begin{aligned} \mathcal{L}_- : \quad & \mathcal{L}_-[x, \Phi_{E_\lambda}(x)]v = (\partial_{xx} - (E_\lambda + \Omega^2) + g\Phi_{E_\lambda}^2(x))v, \\ & v(-L/2) = v(L/2), \quad v'(-L/2) = v'(L/2). \end{aligned}$$

The transformation  $\xi = u + iv$  brings equation (2.30) to a matrix form:

$$\begin{pmatrix} u \\ v \end{pmatrix}_t = \begin{pmatrix} 0 & \mathcal{L}_- \\ -\mathcal{L}_+ & 0 \end{pmatrix} \begin{pmatrix} u \\ v \end{pmatrix} = N \begin{pmatrix} u \\ v \end{pmatrix}. \tag{2.31}$$

This system is a Hamiltonian system that can be written in the form

$$\begin{pmatrix} u \\ v \end{pmatrix}_t = \begin{pmatrix} 0 & 1 \\ -1 & 0 \end{pmatrix} \begin{pmatrix} \mathcal{L}_+ & 0 \\ 0 & \mathcal{L}_- \end{pmatrix} \begin{pmatrix} u \\ v \end{pmatrix} = JH''_{E_\lambda} \begin{pmatrix} u \\ v \end{pmatrix}, \tag{2.32}$$

where for a functional  $F(u, v)$  the notation  $F''(\Phi_{E_\lambda})$  denotes the Hessian matrix  $D^2F(u, v)$  at  $u = \Phi_{E_\lambda}$  and  $v = 0$ . Then  $H''_{E_\lambda}(\Phi_{E_\lambda}) = H''_0(\Phi_{E_\lambda}) - E_\lambda I''(\Phi_{E_\lambda})$  is defined as the Hessian of the energy or the ‘linearized Hamiltonian’, where  $I$  and  $H_0$  are defined by equations (2.2) and (2.4), respectively.

The eigenvalues  $i\omega_j$  of the operator  $N$ ,

$$N \begin{pmatrix} u \\ v \end{pmatrix} = i\omega \begin{pmatrix} u \\ v \end{pmatrix}, \tag{2.33}$$

determine the stability of the particular standing wave. Since the spectrum of  $N$  is symmetric<sup>5</sup> the existence of a non-trivial eigenvalue with a real part (i.e.  $\text{Im}(\omega_j) \neq 0$ ) implies that the standing wave is unstable. Next we repeat, for completeness, the standard calculation of the eigenvalues and the eigenfunctions of  $N$  for the spatially independent quiescent and plane wave solutions. For the other, spatially dependent standing waves, this calculation is too difficult and the explicit solution of the eigenvalue problem is not known. For the inner solutions family, the theory of linear instability [30, 36] and orbital stability of [9, 16, 57] has recently been extended to the periodic problem to establish when they are linearly stable/unstable without explicitly calculating the spectrum of  $N$  [5, 6]. The main steps for establishing these results are included. The stability of the outer solutions family is found by numerical methods as explained below.

*2.2.1. Stability of the quiescent solution.* The linearization (2.30) around the quiescent solution  $\Phi_0(x) = 0, E_\lambda = 0$ ,

$$i\xi_t = \xi_{xx} - \Omega^2\xi \tag{2.34}$$

is solved by  $\xi(x, t) = \hat{\xi}(2\pi j/L)e^{i(\frac{2\pi j}{L}x + \omega t)}$  where  $j \in \mathbb{Z}$ . The eigenvalue problem (2.31) for the operator  $N$  is

$$\det(N - i\omega I) = \begin{bmatrix} -i\omega & -\Omega^2 - \left(\frac{2\pi j}{L}\right)^2 \\ \Omega^2 + \left(\frac{2\pi j}{L}\right)^2 & -i\omega \end{bmatrix} = 0 \tag{2.35}$$

<sup>5</sup> The complex (respectively real) eigenvalues of  $N$  come in quadruples (respectively pairs when  $b = 0$ ):  $i\omega_{1,2,3,4} = \pm a \pm ib$ .

and together with (2.34) leads to the dispersion relation

$$\omega_j^2 = \left( \left( \frac{2\pi j}{L} \right)^2 + \Omega^2 \right). \tag{2.36}$$

The eigenvalues  $i\omega_j$  are always pure imaginary and thus the quiescent solution is linearly stable. The corresponding resonant eigenfunctions  $\Psi(x, t) = \hat{\xi}(2\pi j/L)e^{i(\frac{2\pi j}{L}x + \omega_j t) + iE_0}$  are exactly the linear modes  $\Phi_{E_{\lambda,j}}^{\text{lin}}$  that solve equation (2.18) and satisfy  $E_{\lambda,j} = -\omega_j$ . From these countable infinity linear eigenmodes that are associated with the discrete negative eigenvalues  $E_{\lambda,j}$  emanate the plane wave branch at  $j = 0$  and, for  $j \neq 0$ , the discrete set of the outer solutions  $\Phi_{E_{\lambda,\kappa^j}}^{\text{out}}(x) \xrightarrow[\kappa^j \rightarrow 0]{} \Phi_{E_{\lambda,j}}^{\text{lin}}(x)$ , see figure 4.

2.2.2. *Stability of the plane wave solution.* The linearization (2.30) around the plane wave solution  $\Psi_{\text{pw}} = |c|e^{-iE_{\lambda}^{\text{pw}}t + iE_0}$

$$i\xi_t = \xi_{xx} + 2g|c|^2\xi + g|c|^2\xi^* \tag{2.37}$$

leads to the eigenvalue problem (2.31) for the operator  $N$ :

$$\det(N - i\omega I) = \begin{bmatrix} -i\omega & -(E_{\lambda}^{\text{pw}} + \Omega^2) - \left( \frac{2\pi j}{L} \right)^2 + g|c|^2 \\ (E_{\lambda}^{\text{pw}} + \Omega^2) + \left( \frac{2\pi j}{L} \right)^2 - 3g|c|^2 & -i\omega \end{bmatrix} \tag{2.38}$$

$$= \begin{bmatrix} -i\omega & -\left( \frac{2\pi j}{L} \right)^2 \\ \left( \frac{2\pi j}{L} \right)^2 - 2g|c|^2 & -i\omega \end{bmatrix} = 0, \tag{2.39}$$

which in turn leads to the dispersion relation:

$$\omega_j^2 = \left( \frac{2\pi j}{L} \right)^2 \left( \left( \frac{2\pi j}{L} \right)^2 - 2g|c|^2 \right). \tag{2.40}$$

Hence, for  $(2\pi j/L)^2 < 2g|c|^2$  the plane wave solution is unstable. More generally, plane waves with amplitude  $|c|^2$  in the range

$$I_{\text{pw}} = |c|^2 \in \frac{1}{2g} \left( \frac{2\pi}{L} \right)^2 (j^2, (j+1)^2) = (I_{j\text{LUM}}, I_{(j+1)\text{LUM}}) \tag{2.41}$$

have  $j$  LUM. Namely, the number of linear unstable modes grows linearly with the amplitude. Such instability is called ‘Benjamin–Feir instability’ in the dispersive wave community [8] and ‘modulation instability’ in the plasma physics community [34]. In particular, we will see that for studying the perturbed dynamics it is important to note that for  $I_{\text{pw}} \in (0, I_{1\text{LUM}})$  the plane wave is linearly stable, for  $I_{\text{pw}} \in (I_{1\text{LUM}}, I_{2\text{LUM}})$  the plane wave has only one unstable mode, whereas for  $I_{\text{pw}} > I_{2\text{LUM}}$  the plane wave has at least two unstable modes. Numerically, the linearly stable plane wave solution in the region  $I_{\text{pw}} \in (0, I_{1\text{LUM}})$  appears to be also nonlinearly stable. Analytically, the study of nonlinear stability is beyond the scope of this work; however, it may be studied using methods similar to methods used in the proof of proposition 3.1 in [4], where nonlinear stability of plane wave solutions for the KdV equation was established.

At the bifurcation values  $I_{j\text{LUM}} = (1/2g)(2\pi/L)^2 j^2$ , where  $E_{\lambda,j}^{\text{pw}} = -\Omega^2 + \frac{1}{2} \left( \frac{2\pi}{L} \right)^2 j^2$ , two important structural changes occur in the vicinity of the plane wave branch; first, the interior

linear modes bifurcate from the plane wave family and become the discrete set of the inner solutions branches:  $\Phi_j^{\text{int}}(x; E_\lambda) \xrightarrow{E_\lambda \rightarrow E_{\lambda,j}} \Phi_{E_{\lambda,j}}^{\text{pw}}(x) + \tilde{\Phi}_{E_{\lambda,j}}^{\text{in}}(x)$ . Second, homoclinic orbits to the plane wave are created. These orbits are solutions,  $\Psi_{\text{hom}}(x, t)$ , of the integrable NLS equation such that  $\Psi_{\text{hom}}(x, t) \rightarrow \Psi_{\text{pw}}(t)$  exponentially as  $t \rightarrow \pm\infty$ . The analytic expression for these homoclinic orbits may be found via Bäcklund transformation [17, 23], and their form becomes more and more complex as  $j$ , the number of LUMs, increases. Numerically, the structure of these orbits may be observed by computing quasi-periodic trajectories that are initialized sufficiently close to the plane wave and thus ‘shadow’ the homoclinic structure [17]. Figure 8(c) presents a quasi-periodic solution that shadows a 1-pulse homoclinic orbit of a 1-LUM plane wave solution.

2.2.3. *Stability of the inner (dnoidal) solutions.* It was recently established that the inner standing wave solutions  $\Phi_j^{\text{int}}(x)$  (solutions with  $j$  multiplicity such that their period  $L^{\text{int}} = L/j$ ,  $j \in \mathbb{N}$ ) are stable when  $j = 1$  and are unstable when  $j = 2$ :

**Theorem 1 ([6]).** *The inner standing wave solution  $\Phi_j^{\text{int}}(x)$  with multiplicity  $j = 1$  is orbitally stable, i.e. the orbit  $\mathcal{O}_{\Phi_1^{\text{int}}} = \|e^{i\theta} \Phi_1^{\text{int}}(\cdot + y) : (y, \theta) \in \mathbb{R} \times [0, 2\pi)\|$  is nonlinearly stable. On the other hand,  $\Phi_2^{\text{int}}(x)$  is linearly unstable.*

Below, the instability of  $\Phi_2^{\text{int}}(x)$  is established in a slightly different way: instead of solving explicitly the eigenvalue problem for the operator  $\mathcal{L}_+[x, \Phi_j^{\text{int}}(x)]$  (as in theorem 3.1 of [6]) we establish the instability by invoking the oscillation theorem, the methods introduced in [30] and some intermediate results that are established in [6]. As pointed out also in [6], an immediate consequence of this result is that  $\Phi_j^{\text{int}}(x)$  are unstable for all  $j > 2$ :

**Theorem 2.** *The inner solutions  $\Phi_j^{\text{int}}(x)$  with multiplicity  $j \geq 2$  are linearly unstable.*

**Proof.** Since the spectrum of the operator  $N$  is symmetric with respect to the  $Z_2 \times Z_2$  group, proving the existence of a real eigenvalue implies the existence of a positive real eigenvalue and hence implies instability. In [30] it was shown that it is possible to establish the existence of a real eigenvalue of the operator  $N$  by studying the properties of the eigenvalues of  $\mathcal{L}_-, \mathcal{L}_+$ . Next we list the conditions for instability derived in [30] and show that these conditions are satisfied for the periodic inner standing wave solution with multiplicity  $j \geq 2$ .

The eigenvalue problem for the operators  $\mathcal{L}_-u = \lambda u$ ,  $\mathcal{L}_+v = \lambda v$  with  $L$ -periodic boundary conditions may be viewed as the periodic Hill’s equation

$$y'' + [-\lambda + Q(x)]y = 0 \tag{2.42}$$

depending on a parameter  $-\lambda$  and on a real  $L$ -periodic function  $Q(x)$ . By the Oscillation Theorem (which is based on Floquet theory) for such an equation there are two monotonically decreasing infinite sequences of real numbers [41]

$$\lambda_0, \lambda_1, \lambda_2, \dots, \quad \lambda'_0, \lambda'_1, \lambda'_2, \dots \tag{2.43}$$

where for  $n \in \mathbb{N}$ ,  $\lambda_n$  and  $\lambda'_n$  are the eigenvalues of problem (2.42) with the period  $L$  and period  $2L$ , respectively. The  $\lambda_n$  and  $\lambda'_n$  satisfy the inequalities

$$\dots < \lambda_4 \leq \lambda_3 < \lambda'_4 \leq \lambda'_3 < \lambda_2 \leq \lambda_1 < \lambda'_2 \leq \lambda'_1 < \lambda_0 \tag{2.44}$$

and the eigenfunctions  $y_{2n}$  and  $y_{2n-1}$ , that correspond to the eigenvalues  $\lambda_{2n}$  and  $\lambda_{2n-1}$ , have exactly  $2n$  zeros in the semi-open interval  $x \in [-L/2, L/2)$ . The largest eigenvalue  $\lambda_0$  is always a simple eigenvalue. Its corresponding eigenfunction  $y_0$  has no zeros in the semi-open interval  $x \in [-L/2, L/2)$ . These ordering properties of the eigenvalues and correspondingly

the eigenfunctions with increasing number of zeros are used in lemma 1 to determine the number of positive eigenvalues of the operators  $\mathcal{L}_\pm$ .

**Lemma 1.** Define  $P_j$  and  $Q_j$  as the number of positive eigenvalues of  $\mathcal{L}_+[x, \Phi_j^{\text{int}}(x)]$  and  $\mathcal{L}_-[x, \Phi_j^{\text{int}}(x)]$  with  $j \geq 2$  and with periodic b.c. in  $[-L/2, L/2)$ ,

$$P_j : \# \text{ of positive eigenvalues of } \mathcal{L}_+,$$

$$Q_j : \# \text{ of positive eigenvalues of } \mathcal{L}_-.$$

The numbers  $Q_j$  and  $P_j$  are determined by counting the zeros and the nodes of the standing wave  $\Phi_j^{\text{int}}(x)$ , respectively, in particular

- (a)  $Q_j = 0$ ,
- (b)  $P_j = 2j$  or  $2j - 1$ .

**Proof.**

- (a) Note that  $\Phi_j^{\text{int}}(x)$  on  $x \in [-L/2, L/2]$  satisfies the equation  $\mathcal{L}_-[x, \Phi_j^{\text{int}}(x)]\Phi_j^{\text{int}}(x) = 0$ . Therefore  $\Phi_j^{\text{int}}(x)$  is an eigenfunction of  $\mathcal{L}_-[x, \Phi_j^{\text{int}}(x)]$  with eigenvalue zero. Since  $\Phi_j^{\text{int}}(x)$  is always positive, by the oscillation theorem the zero eigenvalue must be  $\lambda_0$  and therefore  $\forall j, Q_j = 0$ .
- (b) The operator  $\mathcal{L}_+[x, \Phi_j^{\text{int}}(x)]$  is actually the equation of variations of the standing wave equation—it carries the tangent vectors under the flow and therefore the number of nodes of  $\Phi_j^{\text{int}}(x)$  is the number of zeros of  $\Phi_j^{\text{int}}(x)$  that satisfies  $\mathcal{L}_+[x, \Phi_j^{\text{int}}(x)]\Phi_j^{\text{int}}(x) = 0$ . Since the number of nodes of  $\Phi_j^{\text{int}}(x)$  in the semi-open interval  $[-L/2, L/2)$  is  $2j$ , by the oscillation theorem, the eigenvalues that can correspond to the zero eigenvalue are  $\lambda_{2j}$  or  $\lambda_{2j-1}$ . Therefore, it follows that  $P_j = 2j$  or  $2j - 1$ . □

Next we state the parts of the instability theorems [30] that are needed for the proof of theorem 2. The instability theorems connect between  $P_j, Q_j$  and the existence of real eigenvalues of  $N$ . First, define (the dependence on  $j$  enters since  $\mathcal{L}_\pm = \mathcal{L}_\pm[x, \Phi_j^{\text{int}}(x)]$ ):

- $K_j$ —the orthogonal projection on  $(\ker \mathcal{L}_-)^{\perp}$
- $R_j$ —the operator  $R_j = K_j \mathcal{L}_+ K_j$ ,
- $M_j$ —the number of positive eigenvalues of  $R_j$ ,
- $I_{\text{real}}(N_j)$ —the number of pairs of real eigenvalues of  $N_j$ .

**Theorem 3 ([30, 36]).** If  $|M_j - Q_j| = n_j > 0$ , then  $I_{\text{real}}(N_j) \geq n_j$  and thus  $\Phi_j^{\text{int}}(x)$  is linearly unstable.

Define the scalar function  $\vartheta(E_\lambda) = H_0(\Phi_{E_\lambda}) - E_\lambda I(\Phi_{E_\lambda})$ . Differentiating  $\vartheta(E_\lambda)$  twice with respect to  $E_\lambda$ , we receive that the first derivative is  $(d \vartheta(E_\lambda)/dE_\lambda) = \vartheta'(E_\lambda) = -I(\Phi_{E_\lambda})$  and the second is  $(d^2 \vartheta(E_\lambda)/dE_\lambda^2) = \vartheta''(E_\lambda) = -(d/dE_\lambda)[I(\Phi_{E_\lambda})]$ .

**Theorem 4 ([30]).** If  $-\vartheta''(E_\lambda) = (d/dE_\lambda) \frac{1}{L} \int \Phi_{E_\lambda}^2 dx > 0$  along a solution branch  $\Phi_{E_\lambda}$  then  $M = P - 1$ .

**Lemma 2.** For all  $j, -\vartheta''(E_{\lambda,j}) > 0$  along the inner solutions branches  $\Phi_{E_\lambda} = \Phi_j^{\text{int}}(x; E_{\lambda,j})$ .

**Proof.** The proof follows from the derivations and arguments that are presented in [6]. Substituting the expression of  $\Phi_j^{\text{int}}(x; E_{\lambda,j})$  (2.21) into the above integral we obtain

$$-\mathfrak{d}''(E_\lambda) = \frac{d}{dE_{\lambda,j}} \frac{1}{L} \int_{-L/2}^{L/2} \Phi_{E_{\lambda,j}}^2 dx = \frac{2}{gL} \int_{-L/2}^{L/2} \frac{d}{dE_{\lambda,j}} [a_1^2 \mathbf{dn}^2(a_1x, \kappa_j) dx] \tag{2.45}$$

$$= \frac{2a_1}{gL} \left[ 2 \frac{\partial a_1}{\partial E_{\lambda,j}} \int_{-L/2}^{L/2} \mathbf{dn}^2(a_1x, \kappa_j) dx + a_1 \frac{d}{dE_{\lambda,j}} \int_{-L/2}^{L/2} \mathbf{dn}^2(a_1x, \kappa_j) dx \right], \tag{2.46}$$

$$\text{for } a_1^2(E_{\lambda,j}) = \frac{4\pi^2(E_{\lambda,j} + \Omega^2)}{L^2(2 - \kappa_j^2)}. \tag{2.47}$$

Since  $a_1 > 0$  for  $E_\lambda > -\Omega^2$  and the Jacobi-elliptic function  $\mathbf{dn}$  is even and strictly positive the first term is strictly positive. For the second term, it is known that the integral of  $\mathbf{dn}^2$  over its period is expressed by  $E(\kappa_j)K(\kappa_j)$  where  $E$  and  $K$  are elliptic integrals of the second and first kind, respectively. Then the second term becomes  $(d/d\kappa_j)[E(\kappa_j)K(\kappa_j)](d\kappa_j/dE_{\lambda,j})$  and consists of two derivative terms. The first derivative is strictly increasing since it is a derivative with respect to  $\kappa_j$  of a multiplication of two strictly increasing functions for  $\kappa_j \in (0, 1)$ . The second term  $d\kappa_j/dE_{\lambda,j}$  can be shown to be positive as follows. Define a variable  $\eta_2$

$$\eta_2^2 = \frac{2\omega(1 - \kappa^2)}{2 - \kappa^2}, \quad \omega = E_\lambda + \Omega^2$$

Note that  $\eta_2 > 0$  for all  $\kappa \in (0, 1)$ . It is shown in [6] that  $d\eta_2/d\omega < 0$  and a straightforward calculation yields that

$$0 > \frac{d\eta_2}{d\omega} - \frac{1}{2\eta_2} \frac{\partial \eta_2}{\partial \omega} = \frac{1}{2\eta_2} \left( \frac{-4\omega\kappa}{(2 - \kappa^2)^2} \frac{d\kappa}{d\omega} \right)$$

from which we conclude that  $d\kappa/d\omega$  is positive and hence  $-\mathfrak{d}''(E_\lambda)$  is strictly positive. For more details, see [6, equation 3.17].

We conclude that the difference  $n_j = |M_j - Q_j| = 2j - 2$  or  $2j - 1$  must be positive for  $j \geq 2$  and therefore the standing wave solutions  $\Phi_{j \geq 2}^{\text{int}}(x)$  are linearly unstable.  $\square$

**2.2.4. Outer (cnoidal) solutions.** The linear stability of the outer solutions cannot be determined by the above theoretical techniques (see [6] for discussion). In [25] nonlinear (orbital) stability of the small amplitude travelling waves (outer standing and travelling waves) was studied. It was shown that these waves are orbitally stable with respect to perturbations that have the same period and the same Floquet exponent as the original wave, whereas the linearized operator has unstable eigenvalues when general bounded perturbations that are defined on the whole real line and in  $L^2$  or in a real Banach space are considered. The instability is detected for perturbations with wave-numbers that are close to that of the original wave (side-band instability). In [24] the above results are extended to finite amplitude solutions provided a non-degeneracy condition is satisfied (the Hessian matrix needs to have a negative determinant). It is unknown whether this non-degeneracy condition always holds for the outer waves. Here, we determine numerically the linear stability of finite amplitude outer waves in the periodic context, namely with respect to  $L$ -periodic perturbations:

**Conjecture 1.** *The outer solution with a unique oscillation,  $\Phi_1^{\text{out}}(x)$ , is linearly stable for arbitrarily large amplitude, i.e. all eigenvalues of the operator  $N$  lie on the pure imaginary axis.*

*Numerical support.* We calculated the eigenvalues of the operator  $N$  by discretizing the second derivative operator in  $N$  with 4th order Richardson central difference scheme, i.e.  $\mathcal{O}(h^8)$ , where  $h = \frac{1}{256}(2\pi/L)$  is the spatial discretization. The  $\Omega^2$  parameter was set to  $\Omega^2 = 1$  and several  $L$  values were chosen. We computed the eigenvalues of the discretized matrix  $N^d(\Phi_1^{\text{out}}(x))$  for up to  $E_\lambda = 15$  and verified that all the eigenvalues of  $N^d(\Phi_1^{\text{out}}(x))$  are pure imaginary or zero.

These numerical results are consistent with recent theorems that relate the number of eigenvalues with non-negative real part of the operator  $N$  to the number of positive eigenvalues of the self-adjoint symmetric periodic operators  $\mathcal{L}_\pm(\gamma)$ , where the operator  $\mathcal{L}(\gamma)$  is formed by replacing  $\partial x$  in the operator by  $\partial x + i\gamma/L$ , and  $\gamma \in (0, \pi)$  (see [33, 37] and references therein). In particular, divide such eigenvalues to three sets:

$$\sigma_r := \{\lambda \in \sigma(N) : \text{Re}(\lambda) > 0, \text{Im}(\lambda) = 0\},$$

$$\sigma_c := \{\lambda \in \sigma(N) : \text{Re}(\lambda) > 0, \text{Im}(\lambda) \neq 0\},$$

$$\sigma_i := \{\lambda \in \sigma(N) : \text{Re}(\lambda) = 0\}$$

and denote by  $k_l$  the number of eigenvalues belonging to  $\sigma_l$ . Let  $P_j^\gamma$  and  $Q_j^\gamma$  denote the number of positive eigenvalues of the operators  $\mathcal{L}_+(\gamma)$  and  $\mathcal{L}_-(\gamma)$ . Theorem 3.4 in [33] implies that if  $\dim[\text{Ker}(\mathcal{L}_\pm(\gamma))] = 0$  then

$$k_r + k_c + k_i = P_j^\gamma + Q_j^\gamma,$$

$k_c$  and  $k_i$  are always even, and that  $k_r \leq |P_j^\gamma - Q_j^\gamma|$ .

For the outer solutions with  $j = 1$  the above relations become  $k_r + k_c + k_i = 1 + 1$ ,  $k_r = 0$  (as shown in [33]). This relation is inconclusive in terms of determining whether there is a pair of unstable eigenvalues in  $\sigma_c$  or a pair of pure imaginary eigenvalues in  $\sigma_i$ . It does imply that at most one pair can bifurcate from being purely imaginary to the complex spectrum. The numerical results demonstrate that such a bifurcation does not occur at least up to  $E_\lambda = 15$ .

**Conjecture 2.** *The outer solutions  $\Phi_j^{\text{out}}(x)$  with multiplicity  $j \geq 2$  are linearly stable for sufficiently small amplitude, yet, as their amplitude is increased, they lose their stability via a sequence of  $j - 1$  Hamiltonian–Hopf bifurcations; at each such bifurcating solution  $\Phi_{j,m}^{\text{out}}(x)$ ,  $m = 1, \dots, j - 1$ , two distinct purely imaginary pairs (with opposite Krein’s signature) collide, creating a double quadruplet of complex eigenvalues. The amplitude of the  $m$ -th bifurcating solution  $\Phi_{j,m}^{\text{out}}(x)$  increases linearly with both  $k = 2\pi/L$  and  $m$ :  $I_{\text{bif}}^m(\Phi_j^{\text{out}}(x)) = (m^2/g)k^2$ .*

*Numerical support.* See figure 3. For each  $\Phi_j^{\text{out}}(x)$ ,  $j = 2, 3, 4$  we computed the eigenvalues of  $N^d(\Phi_1^{\text{out}}(x))$  for up to  $E_\lambda = 15$  and verified that  $\Phi_j^{\text{out}}(x)$  undergoes  $m = 1, \dots, j - 1$  Hamiltonian–Hopf bifurcations as described above. We then explored the dependence of the bifurcations on the parameter  $L$  and  $\Omega^2$ . While the bifurcations do not depend on  $\Omega^2$  their dependence on  $L$  is  $I_{\text{bif}}^m(\Phi_j^{\text{out}}(x)) = (m^2/g)(2\pi/L)^2$ .

These results are again consistent with the theory presented in [33]. Indeed, as  $j$  increases, the sum of positive eigenvalues  $P_j^\gamma + Q_j^\gamma$  also increases. For outer solutions with multiplicity  $j$  the above relation becomes  $k_r + k_c + k_i = j + j$ ,  $k_r = 0$ . While the relation remains inconclusive with respect to the actual number of unstable eigenvalues, it indeed demonstrates that the number of pairs that may bifurcate to the complex plane increases by one with each increment of  $j$ . Our results show that as  $j$  increases,  $k_r$  remains 0, but the one additional pair of eigenvalues that is added to  $\sigma_r \cup \sigma_i$  bifurcates to the complex plane, i.e. we propose that for  $I > I_{\text{bif}}^{j-1}$ ,  $k_c = 2j - 2$ ,  $k_i = 2$ .

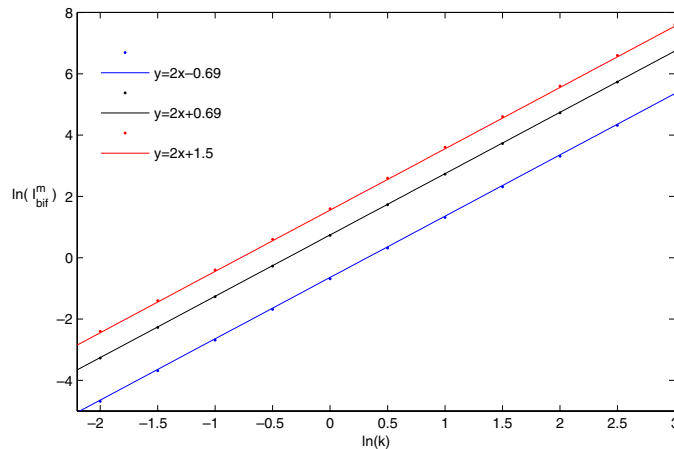


**Figure 3.** The  $m$ th Hamiltonian–Hopf bifurcation.  $I_{\text{bif}}^m(\Phi_j^{\text{out}}(x))$ , the  $m$ -bifurcating amplitudes along the outer solution branches, are shown for increasing wave length  $k$ , at  $m = \{1$  (blue),  $2$  (black),  $3$  (red) $\}$  and  $g = 2$ . The graph suggests that  $I_{\text{bif}}^m(\Phi_j^{\text{out}}(x)) = (m^2/g)k^2$ .

**2.2.5. Travelling waves solutions.** The linear stability of the travelling waves with respect to perturbations that are moving with it (i.e. taking  $\Psi(x, t) = [\Phi'_{E_\lambda}(x', t)e^{-iE'_\lambda t} + \delta\xi(x', t)e^{-iE'_\lambda t}]$ ) is analogous to that of the corresponding standing wave. Indeed, such a linearization of the travelling wave solution yields a linear system as in equation (2.29) where  $x$  is replaced by  $x' = x - vt + s$  and  $E_\lambda$  is replaced by  $E'_\lambda$ . Therefore, the number of zeros and nodes does not change and all the above stability theorems and propositions should apply. It follows that when this travelling-perturbation analysis yields instability, the travelling wave solution is unstable. Establishing stability with respect to arbitrary periodic perturbation is a more subtle issue and is beyond the scope of this work; the linear system becomes

$$i\xi_t = \xi_{xx} - iv\xi_x - (E_\lambda + \Omega^2)\xi + g(2\Phi_{E_\lambda}^2(x - vt + s)\xi + \Phi_{E_\lambda}^2(x - vt + s)\xi^*),$$

which is non-autonomous and other techniques must be employed.

**2.3. Bifurcation diagrams—the PDE-EMBD**

The stability and bifurcations analysis of the standing and the travelling waves solutions of the unperturbed NLS may be geometrically presented by projecting the solution branches onto various observable functionals of the solutions. A common projection is the ‘spectral bifurcation diagram’ by which these solutions are projected to the  $L_2$  and eigenvalue space—the  $(E, I(\Phi_E))$  plane [35]. Here we propose that the projection of these solutions to the two primary constants of motion space, the  $(H_0, I)$  plane, provides a geometric skeleton that is beneficial for studying the structure of nearby integrable solutions and for studying the near-integrable dynamics (see also [58]). We call this projection the PDE-energy–momentum bifurcation diagram (PDE-EMBD). We view it as a natural extension of the traditional EMBDs for finite-dimensional integrable Hamiltonians [7, 20] to the integrable PDE set up.

**2.3.1. Construction of the bifurcation diagram.** The PDE-EMBD is defined as the collection of the special state curves (SSCs), namely the curves  $(h(I), I) = (H_0(\Phi_E), I(\Phi_E))$  created by the projections of the standing waves and travelling waves families onto the  $(H_0, I)$  plane. The spectral diagram consists of the projection of these curves onto the  $(E, I(\Phi_E))$  plane.

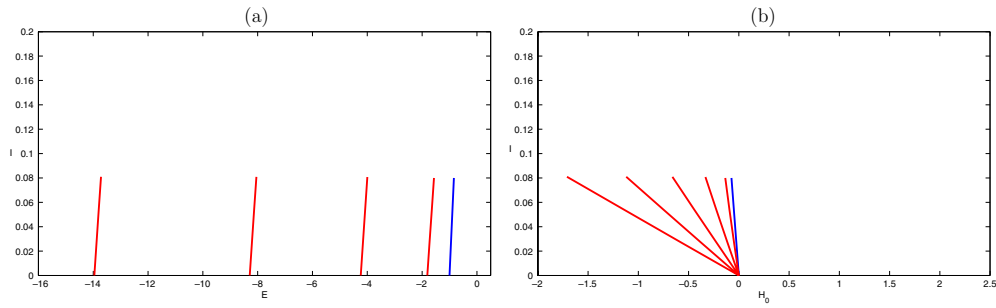


**Figure 4.** The bifurcation diagrams near the quiescent solution. The special solutions curves (SSC) emanate from the quiescent solution (see section 2.2.1): blue—the plane wave mode ( $j = 0$ ), red—all the other outer modes:  $\Phi_{E_\lambda, j}^{\text{lin}}(x)$  with  $j \neq 0$ . (a) The spectral bifurcation diagram (the lines are slanted with a slope  $g$ ). (b) The PDE-EMBD.

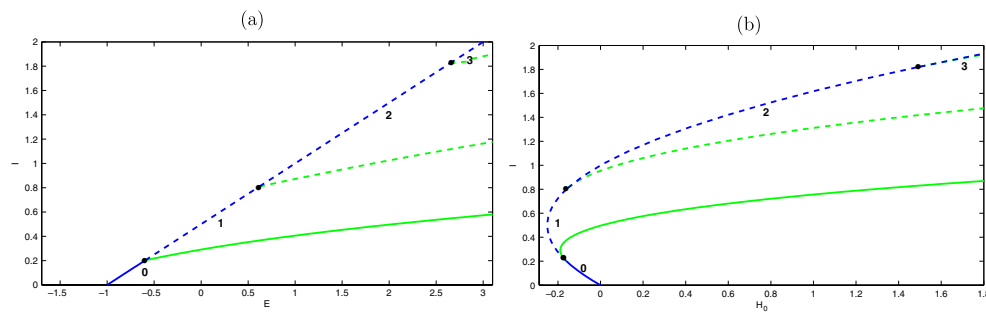


**Figure 5.** The bifurcation diagrams at the plane wave vicinity. The SSC of the plane wave solution (blue) and the bifurcating inner solutions (green) are plotted, with the conventional notation of stability (solid curves—stable, dashed—unstable). The numbers denote the number of families of LUMs. The black dots correspond to parabolic plane waves. (a) The spectral bifurcation diagram. (b) The PDE-EMBD.

The quiescent solution projection onto the PDE-EMBD is the point  $(H_0, I) = (0, 0)$ . Its projection onto the spectral diagram is the full horizontal axis, as  $E$  is arbitrary for the trivial solution. From this quiescent solution a countable set of SSC emerges: the branch of the plane wave and the branches of the outer solutions. In the small amplitude limit, these solutions are well approximated by the linear modes  $\Phi_{E_\lambda, j}^{\text{lin}}$  (section 2.1), and from (2.4)  $H_0(\Phi_{E_\lambda, j}^{\text{lin}}) = E_{\lambda, j} \|\Phi_{E_\lambda, j}^{\text{lin}}\| = E_{\lambda, j} I(\Phi_{E_\lambda, j}^{\text{lin}})$ , so these branches appear as a fan emanating from the origin, see figure 4. The projection of the linearized modes to the spectral diagram is  $(E_\lambda, I) = (-j^2(2\pi/L)^2 - \Omega^2 + gI, I)$ ,  $j \in \mathbb{Z}$ , see figure 4.

The projections of the plane wave branch onto the two different bifurcation diagrams are shown in figure 5 (dark (blue) curve). In the PDE-EMBD it corresponds to the parabola  $(h_{\text{pw}}(I) = (g/2)I^2 - \Omega^2 I, I)$  for  $I \geq 0$  (see equation (2.14)) with an extremum point at  $I = \Omega^2/g$ . In the spectral diagram it corresponds to the line  $(E, I) = (-\Omega^2 + gI, I)$ , for  $I \geq 0$ . For  $I < I_{\text{LUM}}$  the plane wave is stable, and thus its projection appears as a solid curve. For larger  $I$  it is unstable and thus appears as a dashed curve. This dashed curve represents both the plane wave and the homoclinic orbits to it as all these solutions must have the same constants of motion. The plane wave undergoes saddle-center bifurcations at  $I_j = I_{j\text{LUM}}$  (black dots) and from these points the families of inner solutions, bright curves, (in green) are

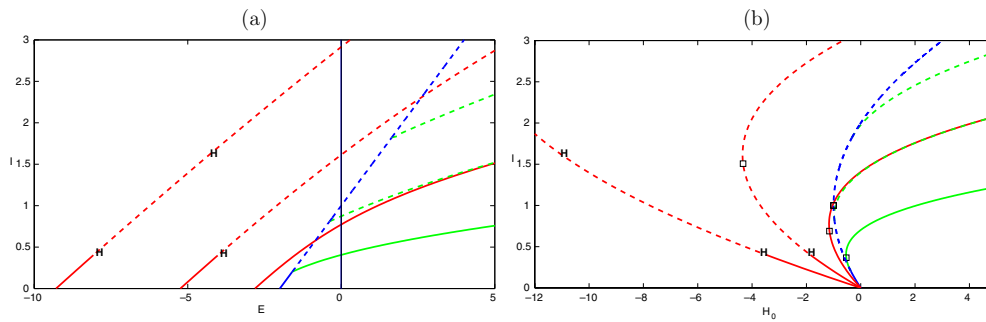


**Figure 6.** Bifurcation diagram of the standing waves solutions up to multiplicity  $j = 3$ . The SSC of the plane wave (blue), outer (red) and inner (green) families of solutions are projected with the conventional notation of stability (solid curves—stable, dashed—unstable). The points at which the outer solutions undergo the Hamiltonian–Hopf bifurcation are marked by ‘H’. (a) The SSC intersections with the vertical line  $E = 0$  in the spectral diagram corresponds to resonant waves. (b) These resonant waves appear as folds of the SSC in the PDE-EMBD and are marked by ‘□’.

emanating. Repeating the same procedure for the outer standing waves and incorporating the stability results of section 2.2 leads to the construction of the full bifurcation diagram shown in figure 6.

Similarly, the travelling waves solutions can be projected to the bifurcation diagrams. Recall that each standing wave solution  $\Phi_{E_\lambda}^{sw}(x; v_m = 0)$  produces a discrete family of travelling wave solutions  $\Phi_{E_\lambda}^{sw}(x'; v_m)$  parametrized by  $v_m, m \in \mathbb{N}$ . These families are projected to the PDE-EMBD (figure 7) by transforming the projections of the standing wave solution  $(H'_0, I', E'_\lambda)$  to  $(H_0, I, E_\lambda)$  according to equations (2.25)–(2.27).

**2.3.2. Resonances.** The standing wave  $\Psi_{sw}(x, t) = e^{-iE_\lambda t + iE_0} \Phi_{E_\lambda}(x)$  is oscillatory in time for  $E_\lambda \neq 0$  and stationary—namely strongly resonant—when  $E_\lambda = 0$ . In general, such resonant solutions are known to produce, even under small perturbations, solutions that have a new structure which is incompatible with the unperturbed dynamics: in section 3 we mainly describe the dynamics near such solutions. Here we note that the resonant standing waves can be easily identified both on the spectral bifurcation diagram and on the PDE-EMBD. In the spectral diagram they simply correspond to the intersection of the standing waves and the vertical line  $E = 0$  as seen in figure 6(a). We next establish that in the PDE-EMBD the resonant standing and travelling waves correspond exactly to the folds of the SSC (marked by an ‘□’ in figure 6(b)):

**Theorem 5.** *Extrema of the SSC  $(h_j(I), I)$  of a standing (respectively travelling) wave family corresponds to the strongest resonance  $E = 0$  (respectively  $E' = 0$ ).*

**Proof.** We prove the theorem first for the standing wave families. We need to show that if there exists an  $I^* = I(\Phi_{E_\lambda})$  such that  $dh_j(I)/dI|_{I=I^*} = 0$  then  $E = 0$ . Indeed, by the chain rule for the standing wave family

$$\frac{dh_j(I)}{dI} = \frac{dH_0[\phi]}{dI} \Big|_{\phi(x)=\phi_j(x)} = H'_0[\phi] \Big|_{\phi(x)=\phi_j(x)} \frac{\delta\phi}{\delta I} \Big|_{\phi(x)=\phi_j(x)},$$

where for integral functionals  $F = 1/L \int_0^L G[x, f(x), f_x(x)]$ ,  $F'[x, f(x), f_x(x)]$  is defined as the functional derivative  $\delta F[\dots]/\delta f$  w.r.t to  $f$ . The rhs vanishes iff  $H'_0[\phi] = 0$ , since  $\phi_j$

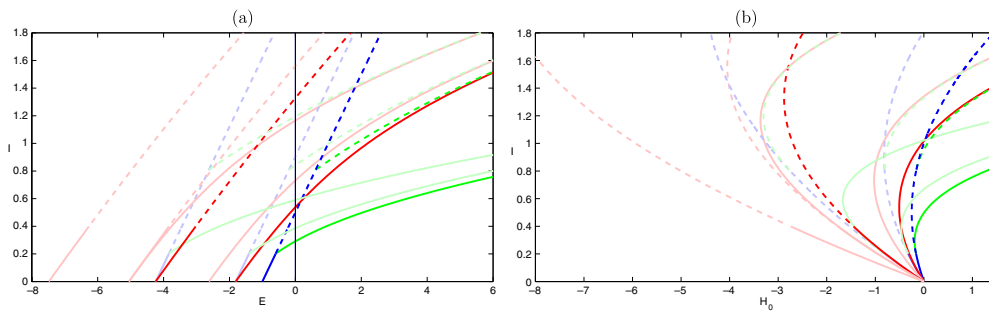


**Figure 7.** Bifurcation diagrams for the standing and travelling waves solutions up to multiplicity  $j = 2$ . Here  $\Omega^2 = 1$  and  $k = 2\pi/L = 0.9$ . The standing waves curves are marked with bold colours and the corresponding travelling waves are marked with opaque colours.

are bounded and for bounded solution  $\phi$  the functional derivative of  $\delta I[\phi]/\delta\phi$  is finite. Since  $\phi_j \in C^\infty$ ,  $H'_0[\phi]$  is zero iff the Euler–Lagrange equation

$$\phi_{xx} - g\phi^3 - \Omega^2\phi = 0$$

is satisfied. This equation is exactly the standing wave equation (equation (2.8)) with  $E = 0$ . Therefore, for the standing wave solutions,  $dh_j(I)/dI = 0$  corresponds to  $E = 0$ .

Similarly, for the SSC  $h_{j,v_k}(I)$  that corresponds to the travelling wave solution  $\phi_{j,v_k}(x')$ , the Euler–Lagrange equation is

$$\phi_{x'x'} - g\phi^3 - \Omega^2\phi = 0$$

that is exactly the travelling waves equation with  $E' = 0$ . Therefore, for the travelling wave solutions,  $dh_{j,v_k}(I)/dI = 0$  corresponds to  $E' = 0$ .  $\square$

In particular, observe that the plane wave solution is resonant at

$$I_{\text{pw-res}} = \Omega^2/g. \quad (2.48)$$

**2.3.3. Integrable solutions: quasi-periodic solutions.** The main advantage of the PDE-EMBD is that the projection of any solution onto this diagram is simple and natural: the functionals  $I$  and  $H_0$  are well defined<sup>6</sup> at any time  $t$  for any function  $\Phi(\cdot, t)$  belonging to the space  $\mathcal{H}^1$ . Moreover, since the unperturbed equation is integrable and  $I$  and  $H_0$  are conserved, any unperturbed solution  $\Phi(x, t)$  projects to the PDE-EMBD as a single point. If this point is bounded away from an SSC then its corresponding profile is distinct from the profiles of the solutions belonging to this family. The key observation here is that for the periodic 1D NLS, the diagram consists of SSCs that are typically well separated (only a few projection-produced overlaps and intersections appear). Hence, it enables to distinguish between neighbourhoods of the different standing waves (and similarly of the travelling waves) solutions. In figure 8 we show different quasi-periodic solutions with the same power (same value of  $I$ ) projected onto the bifurcation diagram.

For most initial profiles, the unperturbed solutions correspond to quasi-periodic motion—these project to a point in the PDE-EMBD. The structure of the quasi-periodic solutions in

<sup>6</sup> In contrast, the projection onto the spectral bifurcation diagram is not well defined for general time-dependent solutions, even in the integrable case, since there is no adequate definition for the nonlinear eigenvalue  $E$ . For example, defining  $E(t)$  as  $K(\Psi(x, t))/I(\Psi(x, t))$  (see equation (2.10)) for the quasi-periodic solutions leads to a time dependent  $E(t)$ .

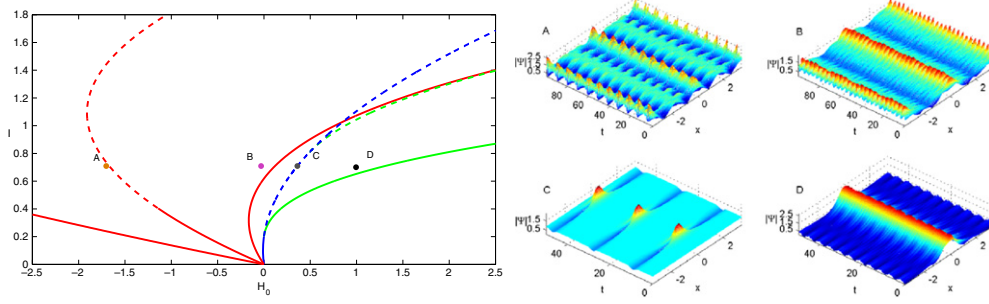


**Figure 8.** Solutions of the integrable equation: surface plots (right) and projections to the PDE-EMBD  $(H_0, I)$  (left).  $I = 0.7$  for all profiles.  $A, B$  lie near the outer 1, 2 multiplicity standing waves,  $C$  lies near the homoclinic orbit of the plane wave and  $D$  lies near the 1 multiplicity inner standing wave.

the neighbourhood of the three types of periodic standing and travelling waves families of solutions (the plane waves, the inner-dnoidal and the outer-cnoidal waves) is nicely organized by the PDE-EMBD skeleton. Quasi-periodic solutions near the stable branches of these SSCs oscillate around them. Quasi-periodic solutions that are located near unstable branches shadow their homoclinic orbits.

Moreover, we show next that the plane wave SSC splits the integrable solutions in its neighbourhood into two distinct families. Consider the near-plane wave family of solutions  $\Psi_{\text{ini-2}}(x, t)$  with two-mode initial data:  $\Psi_{\text{ini-2}}(x, 0) = \Psi_{\text{ini-2}}(x) = [\frac{1}{\sqrt{2}}|c| + (q + ip) \cos(kx + \theta)]e^{i\nu(0)}$ , where  $q, p \in \mathbb{R}$ ,  $0 < |q| + |p| \ll 1$ , and  $qp = 0$ . Denote by  $|c|$  the amplitude of the plane wave solution that has the same power  $I$  as  $\Psi_{\text{ini-2}}(x)$ , and let  $\delta^2 := q^2 + p^2$ :

$$I = \frac{1}{2}|c'|^2 = \frac{1}{2}(|c|^2 + q^2 + p^2) = \frac{1}{2}(|c|^2 + \delta^2). \tag{2.49}$$

We call such solutions with  $\delta \ll 1$  ‘exterior’ if either  $\frac{1}{2}|c'|^2 \leq I_{\text{ILUM}}$  or  $\{\frac{1}{2}|c'|^2 > I_{\text{ILUM}}$  and  $p \neq 0\}$ , and ‘interior’ if  $\{\frac{1}{2}|c'|^2 > I_{\text{ILUM}}$  and  $q \neq 0\}$  (this definition is motivated by the structure of the truncated model, see section 3.1). We now establish:

**Theorem 6.** *The projections of ‘exterior’ (respectively ‘interior’) solutions to the PDE-EMBD are to the left (respectively to the right) of the plane wave SSC.*

**Proof.** Since we consider the integrable dynamics the constants of motion are preserved and hence  $I(\Psi_{\text{ini-2}}(x, t)) = I_2(|c|, q, p) := \frac{1}{2}(|c|^2 + q^2 + p^2)$  and similarly  $H_0(\Psi_{\text{ini-2}}(x, t)) = H_{0,2}(|c|, q, p)$  where

$$H_{0,2}(|c|^2, q, p) = -\frac{k^2}{2}(q^2 + p^2) + \frac{g}{8}|c|^4 + \frac{3g|c|^2q^2}{4} + \frac{g|c|^2p^2}{4} + \frac{3g(q^2 + p^2)^2}{16} - \frac{\Omega^2|c|^2}{2} - \frac{\Omega^2(q^2 + p^2)}{2}.$$

To prove the theorem, we need to show that for the exterior solutions  $H_{0,2}(|c|^2, q, p) < H_0(|c'|^2, 0, 0)$  whereas for the interior solutions the opposite inequality holds. First, note that

$$H_{0,2}(|c'|^2, 0, 0) = \frac{g}{2}(I)^2 - \Omega^2 I = \frac{g}{8}|c|^4 + \frac{g|c|^2\delta^2}{4} - \frac{\Omega^2|c|^2}{2} - \frac{\Omega^2\delta^2}{2} + \frac{g}{8}\delta^4.$$

Now, for the exterior orbits with  $p \neq 0$  we have

$$\begin{aligned} H_{0,2}(|c|^2, 0, \delta) &= -\frac{k^2\delta^2}{2} + \frac{g|c|^2\delta^2}{4} + \frac{g}{8}|c|^4 - \frac{\Omega^2|c|^2}{2} - \frac{\Omega^2\delta^2}{2} + \frac{3g\delta^4}{16} \\ &= H_{0,2}(|c'|^2, 0, 0) - \frac{k^2\delta^2}{2} + \frac{g\delta^4}{16} < H_{0,2}(|c'|^2, 0, 0), \end{aligned}$$

where the last inequality holds for sufficiently small  $\delta$  ( $\delta^2 < (8k^2/g)$ ), so the theorem is established for such solutions. The exterior orbits with  $q \neq 0$  also satisfy, by definition,  $\frac{1}{2}|c|^2 + \frac{1}{2}\delta^2 \leq (k^2/2g) = I_{\text{ILUM}}$  and thus

$$\begin{aligned} H_{0,2}(|c|^2, \delta, 0) &= -\frac{k^2\delta^2}{2} + \frac{3g|c|^2\delta^2}{4} + \frac{g}{8}|c|^4 - \frac{\Omega^2|c|^2}{2} - \frac{\Omega^2\delta^2}{2} + \frac{3g\delta^4}{16} \\ &= H_{0,2}(|c'|^2, 0, 0) + \delta^2 \left( -\frac{k^2}{2} + \frac{g|c|^2}{2} \right) + \frac{g\delta^4}{16} \\ &\leq H_{0,2}(|c'|^2, 0, 0) - \frac{7g\delta^4}{16} < H_{0,2}(|c'|^2, 0, 0), \end{aligned}$$

as claimed. Finally, this last inequality is reversed for interior orbits; Indeed, the above calculation shows that  $H_{0,2}(|c|^2, \delta, 0) > H_{0,2}(|c'|^2, 0, 0)$  provided  $\delta^2 > (16/g)((k^2/2) - (g|c|^2/2))$ . Utilizing the definition of  $c'$  (equation (2.49)) we obtain that this inequality is satisfied when  $\delta^2 < \frac{16}{7}((|c'|^2/2) - (k^2/2g))$ , namely that for  $(|c'|^2/2) > I_{\text{ILUM}}$  and sufficiently small  $\delta$  the reverse inequality indeed holds.  $\square$

### 3. The near-integrable dynamics

Consider now the perturbed NLS equation, namely equation (1.2). In the autonomous frame ( $\Psi = \varphi e^{i\Omega^2 t - i\alpha}$ ) the equation becomes

$$i\Psi_t - \Psi_{xx} - (g|\Psi|^2 - \Omega^2)\Psi = \varepsilon - i\delta\Psi, \quad (3.1)$$

where  $\varepsilon$  is the forcing amplitude,  $\delta$  is the damping coefficient and  $\varepsilon, \delta \ll 1$ . We will mostly concentrate here on the forced (undamped) equation ( $\delta = 0, \varepsilon \neq 0$ ). This equation is conservative, as the total Hamiltonian

$$H_T(\Psi) = H_0(\Psi) + \varepsilon H_1(\Psi), \quad H_1(\Psi) = \frac{1}{L} \int (\Psi^* + \Psi) dx \quad (3.2)$$

is preserved (whereas the damping term dissipates the energy).

The forced system is chaotic and exhibits rich behaviour. Since there is no dissipation of energy, regular, temporal chaotic and spatio-temporal chaotic solutions co-exist. We propose that there are three useful projections of the solutions that are helpful in distinguishing between distinct solutions: projections onto the PDE-EMBD, the phase–power projection and the  $qp$  projection. These projections are motivated by the study of a two-mode truncation of the forced NLS, a model that turned out to contribute much to our understanding of the evolution of solutions with the initial nearly flat low-amplitude profile [51, 52]. We thus review next the construction of the two-mode model and explain what are the phase–power and the  $qp$  projections. We then use these projections to explain the phase-space structure of the perturbed PDE dynamics near the plane waves, demonstrating that the projections allow us to distinguish between various types of solutions. We end this section by analysing one of the recently discovered chaotic solutions—the parabolic resonant type: we show that the truncated model may be used to predict the extent of the instabilities associated with this solution.

### 3.1. The two degrees of freedom model

The two degrees of freedom (d.o.f) truncated model of the forced NLS was proposed in [10, 12, 38] as a simplified phenomenological model to characterize some of the observed near-integrable dynamics of the NLS PDE and was studied in [31, 38, 51]. The model is derived by substituting in the forced NLS the finite expansion<sup>7</sup>,

$$\Psi_{N+1}(x, t) = \frac{1}{\sqrt{2}} |c(t)| e^{i\gamma(t)} + b(t) e^{i\gamma(t)} \cos(kx) + a_1(t) e^{i\gamma(t)} \sin(kx) + \sum_{n=2}^N (a_n(t) e^{i\gamma(t)} \sin(knx) + b_n(t) e^{i\gamma(t)} \cos(knx)),$$

truncating the equations at  $N = 1$ , and considering only symmetric initial profiles (setting  $a_1(t) = 0$ ), see [32, 38, 51]. While there is not yet a rigorous justification for this crude truncation, it appears to provide a fairly accurate description of the PDE dynamics near the plane waves as long as  $I$ , the  $L_2$  norm of the solution, satisfies  $I < I_{2\text{LUM}}$  [10–12, 17, 52]. Indeed, near the plane wave, linear stability (equation (2.40)) shows that the higher modes  $\cos(nkx)$ ,  $\sin(nkx)$ ,  $n = 2, \dots, \infty$  are stable with frequency  $\omega_n = \sqrt{(2\pi n/L)^4 - 2g(2\pi n/L)^2 |c|^2} = \mathcal{O}(n^2)$ , and thus, in the non-resonant case, can be treated as stable oscillators. Since these modes are much faster than the first and the second modes (the frequency increases as  $n^2$ ), one expects that resonances will be rare and that the slow dynamics will essentially decouple from the fast modes (see [22, 26] for related results). The resulting truncated system is a near-integrable two d.o.f Hamiltonian of the form  $\bar{H}(b, c) = \bar{H}_0(b, c) + \varepsilon \bar{H}_1(b, c)$ , where, in the integrable limit ( $\varepsilon = 0$ ),  $\bar{I} = \frac{1}{2}(|c|^2 + |b|^2) = \|\Psi_2(x)\|_{L_2}$  is preserved.

**3.1.1. The integrable system.** The first main step in the analysis of the truncated integrable dynamics ( $\varepsilon = 0$ ) is a transformation from the Fourier mode amplitudes  $(c, b)$  to the generalized action-angle coordinates  $(q, p, \bar{I}, \gamma)$  [38]:

$$c = |c| \exp(i\gamma), \quad b = (q + ip) \exp(i\gamma), \quad (3.3)$$

$$\bar{I} = \frac{1}{2}(|c|^2 + q^2 + p^2). \quad (3.4)$$

The transformation brings the Hamiltonian  $\bar{H}_0(b, c)$  to the form

$$\begin{aligned} \bar{H}_0(q, p, \bar{I}; \Omega^2, k^2, g) &= \frac{g}{2} (\bar{I})^2 - \Omega^2 \bar{I} + \left( g \bar{I} - \frac{1}{2} k^2 \right) q^2 - \frac{7g}{16} q^4 - \frac{3g}{8} q^2 p^2 \\ &+ \frac{g}{16} p^4 - \frac{1}{2} k^2 p^2, \end{aligned}$$

where

$$(\bar{I}, \gamma) \in (R^+ \times T), \quad (q, p) \in B_{\bar{I}} = \{(q, p) | q^2 + p^2 < 2\bar{I}\}$$

and the truncated model depends on the two parameters  $\Omega^2$  and  $k = 2\pi/L$ . The two truncated integrals of motion  $\bar{H}_0$  and  $\bar{I}$  are analogous to  $H_0$  and  $I$  of the PDE.

Once these coordinates are introduced<sup>8</sup>, the structure of the unperturbed solutions and the structure of the unperturbed energy surfaces may be easily found. Since  $\bar{I}$  is a constant of motion and  $\bar{H}_0$  is independent of  $\gamma$ , for any given  $\bar{I}(0)$  the Hamiltonian  $\bar{H}_0(q, p, \bar{I}(0))$  may be viewed as a one-degree of freedom Hamiltonian (we refer to it as the reduced Hamiltonian) that

<sup>7</sup> Here  $c(t)$ ,  $b(t)$ ,  $b_n(t)$ ,  $a_n(t)$  are complex functions and  $\gamma(t)$  is the phase of  $c(t)$ .

<sup>8</sup> Notice though that, as opposed to regular action-angle coordinates, the velocity of  $\gamma$  along the unperturbed quasi-periodic trajectories is usually non-constant.

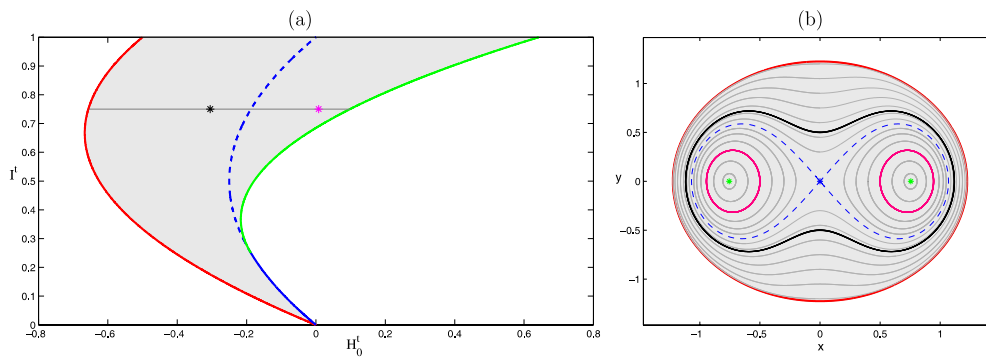


**Figure 9.** The structure of the two d.o.f model ( $k = 1$ ,  $\Omega^2 = 1$ ,  $g = 2$ ). (a) The EMBD: the grey area denotes the allowed region of motion, the coloured curves denote the families of the singular circles. (b) The  $(q, p)$  phase plane at  $I = 0.75$  (the horizontal line in the EMBD). The projections of perturbed regular interior (magenta) and regular exterior (black) solutions onto the EMBD and onto the  $qp$  plane are shown.

controls the motion in the  $(q, p)$  plane, namely, the motion occurs along the closed  $qp$ -level<sup>9</sup> sets of  $\bar{H}_0(q, p, \bar{I})$ . The topology of the level sets of the truncated two d.o.f. system may be easily found: for  $(q, p) \in B_I$ , each  $qp$ -level set is crossed with a circle of phases  $\gamma$ . For  $\bar{I} < I_{\text{ILUM}}$ , the reduced Hamiltonian has a single elliptic fixed point at the origin (corresponding to the plane wave solution and denoted by  $(q_f^{\text{pw}}, p_f^{\text{pw}}) = (0, 0)$ ) and all the other  $qp$ -level sets of  $\bar{H}_0(q, p, \bar{I})$  are regular and diffeomorphic to circles that encircle it. Thus for  $\bar{I} < I_{\text{ILUM}}$ , the level sets of the two d.o.f. system correspond to a single torus, with only two exceptions of singular level sets that correspond to a circle: the  $qp$  origin multiplied by a circle of phases  $\gamma$  and the boundary of  $B_I$  (namely, the circle  $q^2 + p^2 = 2\bar{I}$ , where  $c(t) = 0$  and  $\gamma$  is not defined).

At  $I_{\text{ILUM}}$  the origin undergoes a pitchfork bifurcation, so that for  $\bar{I} \in (I_{\text{ILUM}}, I_{2\text{LUM}})$  the reduced Hamiltonian has a figure eight structure (see figure 9(b)). The regular level sets of the two d.o.f. system correspond to either a single torus (for exterior  $qp$ -orbits, namely orbits in the  $qp$  plane that encircle the figure eight) or to two disconnected tori (for interior  $qp$ -orbits, one in each of the figure eight loops, see figure 9(b)). These  $qp$  plots motivated the PDE definition of interior and exterior orbits that appear in theorem 6. For these values of  $\bar{I}$  there are four singular level sets: the circle corresponding to the boundary of  $B_I$ , the two circles corresponding to the elliptic points inside the figure eight, and the two-dimensional level set that corresponds to a circle in  $\gamma$  crossed with the  $qp$ -figure eight.

The above description provides a full characterization of the level sets of the Hamiltonian for any fixed  $\bar{I} < I_{2\text{LUM}}$ . To obtain from it the structure of the energy surfaces, which is instrumental for providing a qualitative prediction of the perturbed dynamics as explained next, we construct the energy–momentum bifurcation diagram (EMBD) [7, 20, 39, 40, 51, 54]. In this bifurcation diagram we plot, in the plane of  $(\bar{H}_0, \bar{I})$ , the singular curves—the curves that correspond to the singular level sets. Namely, we plot  $h_s(\bar{I}) = (\bar{H}_0(q_f(\bar{I}), p_f(\bar{I}), \bar{I}), \bar{I})$ , where  $(q_f(\bar{I}), p_f(\bar{I}))$  stand for either one of the three fixed points in the  $(q, p)$  plane or to the boundary of  $B_I$ . The region of allowed motion is the region bounded between the stable curves in the EMBD (grey region in figure 9(a)). Every point that belongs to the allowed region of motion corresponds to a single level set, which may have either one or two components. The energy surface  $\bar{H}_0(q, p, \bar{I}, \gamma; \Omega^2, k^2, g) = h$  corresponds to the intersection of a vertical line  $\bar{H}_0 = h$  with the grey region in this diagram.

<sup>9</sup> i.e. the level set of  $\bar{H}_0(q, p, \bar{I}(0))$  in the  $(q, p)$  plane.

Points along this energy surface line that do not belong to the singular curves correspond to regular level sets. The motion on these level sets is generically quasi-periodic, yet there are dense set of points on which the motion is resonant (namely, there exist  $n, m \in \mathbb{Z}$  with  $|n| + |m| \neq 0$ , so that the two frequencies that arise obey  $n\omega_1 + m\omega_2 = 0$ ). Similarly, the motion on the singular level sets, which are composed of circles, is called resonant if the normal frequency (the imaginary eigenvalues of the linearized reduced Hamiltonian at the  $qp$ -fixed points) and the frequency of the motion along the circle ( $\dot{\gamma}|_{\{q_f, p_f, \bar{I}\}}$ ) are resonant. The strongest resonant circle<sup>10</sup> thus appears when  $\dot{\gamma}|_{\{q_f, p_f, \bar{I}^{\text{res}}\}} = 0$ . Then,  $(q_f, p_f, \bar{I}^{\text{res}}, \gamma)$  is a circle of fixed points (see [38, 51]). In fact, such a circle of fixed points always corresponds to an extremum of the singular curves, namely  $dh_s(\bar{I})/d\bar{I} = 0$  exactly at such a resonant circle (and therefore the foliation of the energy surface changes at such points, see [48, 51]). For the plane wave solution, such a circle of fixed points appears at

$$\bar{I}^{\text{res}} = \frac{\Omega^2}{g}, \tag{3.5}$$

the same power at which the PDE plane wave is resonant, see equation (2.48).

Finally, note that the singular plane wave curve ( $h_s^{\text{pw}}(\bar{I}) = (\bar{H}_0(0, 0, \bar{I}), \bar{I})$ ) splits the neighbourhood of the plane wave into two distinct regions: to the right of the plane wave the quasi-periodic solutions follow the ‘interior’ part of the homoclinic solution in the  $(q, p)$  plane and each level set is composed of two-tori. The solutions to the left of the plane wave curve follow the ‘exterior’ part of the homoclinic orbit and the level set corresponds to a single torus. Theorem 6 shows that provided the initial profile has all of its power in the first two modes (so  $\Psi(x, 0) = \Psi_{\text{ini-2}}(x)$ ), the PDE-EMBD inherits this property as well (similar property is expected to hold for initial data with sufficiently rapid decay of higher modes).

3.1.2. *The near-integrable system.* Now consider the perturbed truncated system:

$$\bar{H}(q, p, \bar{I}, \gamma) = \bar{H}_0(q, p, \bar{I}) + \varepsilon \bar{H}_1(q, p, \bar{I}, \gamma), \tag{3.6}$$

where

$$\bar{H}_1(q, p, \bar{I}, \gamma) = \sqrt{2} \sqrt{2\bar{I} - q^2 - p^2} \sin \gamma. \tag{3.7}$$

The solution structure of the resulting two d.o.f near-integrable system depends on the parameters  $(L, \Omega; g)$ , the energy level, and the phase-space region (we consider here only the PDE relevant region,  $I \leq I_{2\text{LUM}}$ ) and are roughly divided into regular and chaotic solutions.

*Regular solutions.* In the limit of small  $\varepsilon$ , by the KAM theorem, most initial conditions evolve as quasi-periodic solutions. We call such solutions regular solutions. The regular quasi-periodic solutions are either  $\varepsilon$ -close to some unperturbed solutions (the non-resonant case) or may correspond to quasi-periodic motion surrounding resonant periodic solutions with  $\bar{I}$  variations of order  $\sqrt{\varepsilon}$  (KAM tori of the partially averaged system near resonances). These solutions appear for typical initial data  $(q_i, p_i, \bar{I}_i, \gamma_i)$  belonging to the regions of the EMBD that are at least  $\varepsilon$  away from the unstable part of the singular plane wave curve (i.e. for all  $\bar{I}_i \in (I_{1\text{LUM}}, I_{2\text{LUM}})$ , we take  $|\bar{H}_0(q_i, p_i, \bar{I}_i) - h_s^{\text{pw}}(\bar{I}_i)| > \mathcal{O}(\varepsilon)$ ):

*Non-resonant elliptic solutions.* The EMBD region to the left of the plane wave curve  $h_s^{\text{pw}}(\bar{I})$  at small  $\bar{I}$  values ( $\bar{I} < I_{1\text{LUM}}$ ), corresponds, in the unperturbed case, to elliptic orbits:  $qp$  orbits that encircle the origin and appear as horizontal lines in the  $(\gamma, \bar{I})$  plane. The non-resonant perturbed trajectories follow  $\varepsilon$ -closely such integrable trajectories in both  $(q, p)$  and  $(\gamma, \bar{I})$

<sup>10</sup> The smaller is  $|n| + |m|$ , the stronger is the resonance.

planes. On the EMBD, such perturbed solutions cover, in a regular pattern, a square of width  $\mathcal{O}(\varepsilon)$  to the left of the plane wave curve.

*Non-resonant exterior solutions.* The EMBD region to the left of the plane wave curve  $h_s^{\text{pw}}(\bar{I})$  with  $\bar{I}$  in the unstable regime ( $I_{1\text{LUM}} < \bar{I} < I_{2\text{LUM}}$ ), corresponds, in the unperturbed case, to exterior orbits:  $qp$  orbits that encircle the figure eight homoclinic orbit associated with  $\bar{I}$  and appear as horizontal lines in the  $(\gamma, \bar{I})$  plane. The typical perturbed solutions with initial data in this region (that is  $\varepsilon$ -away in  $H_0$  from  $h_s^{\text{pw}}(\bar{I})$ ), follow the unperturbed dynamics exactly as in the elliptic case, see, e.g. the outer to the homoclinic orbit (black) trajectory in figure 9(b).

*Non-resonant interior solutions.* The EMBD region to the right of the plane wave curve  $h_s^{\text{pw}}(\bar{I})$  with  $\bar{I}$  in the unstable regime ( $I_{1\text{LUM}} < \bar{I} < I_{2\text{LUM}}$ ), corresponds, in the unperturbed case, to interior orbits:  $qp$  orbits that are inside the right or left part of the figure eight homoclinic orbit associated with  $\bar{I}$ . The corresponding regular perturbed solutions (namely solutions with initial data that project to the same region of the EMBD) follow the unperturbed dynamics, see, e.g. the interior to the homoclinic orbit (magenta) trajectory in figure 9(b).

*Regular resonant solutions.* When a resonance occurs at a regular level set, namely an unperturbed two torus is resonant, a resonance region of  $\mathcal{O}(\sqrt{\varepsilon})$  is created in the  $(\tilde{\gamma}, \bar{I})$  plane, where  $\tilde{\gamma}$  denotes the resonant phase angle. The perturbed solutions follow the level lines of the partially averaged Hamiltonian in the  $(\tilde{\gamma}, \bar{I})$  plane (slow pendulum-like dynamics) while encircling (fast dynamics) the corresponding  $qp$ -level set. By the KAM theorem for the partially averaged Hamiltonian, most solutions in this region are quasi-periodic, and the exceptional set is exponentially small (we disregard this exceptional set in our classification). Projecting such solutions to the EMBD produces a rectangle of  $H$ -width of  $\mathcal{O}(\varepsilon)$  and  $I$ -height of  $\mathcal{O}(\sqrt{\varepsilon})$ . In particular, the resonant solutions in the flat plane, where  $b(0) = b(t) = 0$ , may be easily found; On this invariant plane:

$$\bar{H}(0, 0, \bar{I}, \gamma) = \frac{g}{2}(\bar{I})^2 - \Omega^2 \bar{I} + 2\varepsilon\sqrt{\bar{I}} \sin \gamma, \tag{3.8}$$

so the half-width of the resonance zone near  $\bar{I}^{\text{res}}$ , in which regular oscillatory motion in  $\gamma$  occurs, is

$$\Delta \bar{I} = \frac{2}{\sqrt{g}} \sqrt{\frac{\Omega \varepsilon}{\sqrt{g}}}. \tag{3.9}$$

*Chaotic solutions.* Solutions with typical initial data  $(q_i, p_i, \bar{I}_i, \gamma_i)$  near the unstable branch of the plane wave exhibit chaotic behaviour. Three observable<sup>11</sup> chaotic mechanisms associated with the appearance of homoclinic orbits at  $I \geq I_{1\text{LUM}}$  (see figure 3 in [52] and figure 11 of section 3.2 for the similar PDE projections to the PDE-EMBD) appear:

*Homoclinic chaos.* For any given  $\delta$ , for sufficiently small  $\varepsilon$ , solutions with typical initial data chosen close to the homoclinic orbits with  $\bar{I}_i \in (I_{1\text{LUM}}, I_{2\text{LUM}}) \setminus [\bar{I}^{\text{res}} - \delta, \bar{I}^{\text{res}} + \delta]$  evolve chaotically in the  $(q, p)$  plane as in periodically forced one d.o.f systems. Since  $\dot{\gamma}_{(0,0,\bar{I}(t))} \neq 0$  for such solutions, the section  $\gamma = \gamma_0$  provides a local Poincaré map near the corresponding hyperbolic circle, and thus transverse intersections of the circles' stable and unstable manifolds with  $\mathcal{O}(\varepsilon)$  splitting angle may be established by standard methods. Thus, we say that such chaotic solutions are created by the standard homoclinic chaos mechanism. Away from the singular circle the motion in  $\gamma$  may be non-monotone, yet, in the non-resonant cases, the

<sup>11</sup> We disregard here the complicated behaviour which includes chaotic motion in the exponentially small regions near resonances boundaries.

distribution of  $\gamma$  values along chaotic trajectories appears to be uniform (islands of stability in the homoclinic region may destroy this uniformity in  $\gamma$ ). The projection of such solutions onto the EMBD appears as almost horizontal lines (with slope of  $\mathcal{O}(\varepsilon)$ ) that occasionally cross the plane wave curve  $h_s^{\text{pw}}(\bar{I})$ . Eventually, the projection covers, in an irregular way, a square of width  $\mathcal{O}(\varepsilon)$  near the initial data projected point  $(H_0(q_i, p_i, \bar{I}_i, \gamma_i), \bar{I}_i)$ .

*Hyperbolic resonance.* Solutions with typical initial data chosen close to the homoclinic orbit of a resonant hyperbolic circle, namely, with  $\bar{I}_i = \bar{I}^{\text{res}} + \mathcal{O}(\sqrt{\varepsilon})$  exhibit chaotic behaviour which is of essential different characters than the standard homoclinic chaos [31, 32, 38]. Note that such solutions appear only when the resonant plane wave is unstable ( $\bar{I}^{\text{res}} > I_{\text{ILUM}}$ ), namely, when  $\Omega^2 > \Omega_{\text{PR}}^2 = k^2/2$ . Away from the  $q = p = 0$  invariant plane, such orbits follow the homoclinic loop, whereas near this plane they shadow the resonant slow pendulum-like dynamics in the  $(\gamma, I)$  plane. Thus, in this case the variations in  $\bar{I}$  are of  $\mathcal{O}(\sqrt{\varepsilon})$ . On the EMBD, the projection of such solutions appears as almost horizontal lines with occasional fast  $\mathcal{O}(\sqrt{\varepsilon})$  drops in  $\bar{I}$ , covering eventually a rectangle of width  $\mathcal{O}(\varepsilon)$  and height  $\mathcal{O}(\sqrt{\varepsilon})$  near  $(H_0(q_i, p_i, \bar{I}_i, \gamma_i), \bar{I}_i)$ .

*Parabolic resonance.* Near the critical parameters value  $\Omega^2 \approx (k^2/2)$  (where  $\bar{I}^{\text{res}} \approx I_{\text{ILUM}}$ ), typical solution with initial data in the neighbourhood of the nearly parabolic and nearly resonant plane wave exhibit intermittent chaotic behaviour. The projection of such solutions to the EMBD appears to oscillate along the parabola-shaped lines, changing their fidelity as these lines cross the plane wave curve  $h_s^{\text{pw}}(\bar{I})$ . These projections cover eventually an arched shape region of width  $\mathcal{O}(\varepsilon)$  and height  $\mathcal{O}(\sqrt{\varepsilon})$  near  $(H_0(q_i, p_i, \bar{I}_i, \gamma_i), \bar{I}_i)$ . Following [50], we show in section 3.3 that the parabola-like level lines correspond to an adiabatic invariant that is preserved by the perturbed trajectories as long as they are away from the plane wave separatrices, namely their projection is away from the curve  $h_s^{\text{pw}}(\bar{I})$ .

### 3.2. The perturbed PDE phase-space structure near the plane waves

The nonlinear chaotic nature of the truncated system suggests that a standard comparison between perturbed and unperturbed solutions of the PDE (e.g. plotting time integral of the  $L_2$  norm of the difference between the solutions) will not be informative. Instead, we seek qualitative comparison between the solutions. These are achieved by comparing the three projections that were introduced in the two d.o.f analysis, where the generalized action-angle coordinates  $(q, p, \bar{I}, \gamma)$  were naturally defined. Denote by  $C_n \Psi(x, t) = \hat{\Psi}(n, t)$  the  $n$ th complex coefficient of the Cosine tranform of the solutions ( $C_n \Psi(x, t) = \frac{1}{L} \int_{-L/2}^{L/2} \Psi(x, t) \cos(nkx) dx$ ), and define the following three projections of the PDE solutions:

- (P1) *Projection onto the PDE-EMBD.* We plot the parametric curve  $\{\zeta_t\}_{t \in [0, \tau]}$  where  $\zeta_t = (H_0(\Psi(x, t)), I(\Psi(x, t)))$  (recall equations (2.2) and (2.4)) on top of the skeleton of the projections of the unperturbed standing and travelling wave solutions. Note that by (3.2) the curve  $\{\zeta_t\}_{t \in [0, \tau]}$  always (for all  $\tau$ ) projects into a strip of width  $\mathcal{O}(\varepsilon)$  in  $H_0$  around the initial energy  $H_0(\Psi_0(x))$ .
- (P2) *Projection onto the phase–power plane.* We plot the parametric curve  $\{\rho_t\}_{t \in [0, \tau]}$  in the  $(\gamma, I)$  plane, namely we plot  $\rho_t = (\gamma(t), I(\Psi(x, t)))$ . Here  $\gamma(t) = \arg C_0 \Psi(x, t)$  is the phase of the flat part of the solution.
- (P3) *Projection onto the  $(q, p)$  plane.* We plot the parametric curve  $\{\xi_t\}_{t \in [0, \tau]}$  in the  $(q, p)$  plane, where  $(q, p)$  are defined as the real and imaginary parts of the first mode of the solution (phase shifted to match the flat phase):

$$\xi_t = (\text{Re}[C_1 \Psi(x, t)e^{-i\gamma(t)}], \text{Im}[C_1 \Psi(x, t)e^{-i\gamma(t)}]). \tag{3.10}$$

We show that these projections reveal, on the one hand, the analogy between the ODE and the PDE solutions, and on the other hand, enable to detect when the PDE behaviour is distinct from the ODE. A few notes are in order:

1. These projections hide the explicit time dependence of the solutions, as appropriate for the qualitative comparison between perturbed and unperturbed solutions.
2. Note that the first projection uses the integrable PDE structure as an underlying skeleton for the motion, thus providing accurate division of the projected PDE space to interior and exterior solutions for initial data that is located near the plane wave and has only two modes (recall theorem 6).
3. Below, we utilize our understanding of the dynamics associated with the family of two-mode *initial data*:

$$\Psi_0(x) = \Psi_{\text{ini-2}}(x) = \left[ \frac{1}{\sqrt{2}}|c| + b(0) \cos(kx) \right] e^{i\gamma(0)}. \quad (3.11)$$

It appears that adding to such initial profiles higher modes that decay rapidly does not change the qualitative statements regarding the dynamics (yet may shift the SCC curves).

4. Note that two-mode initial data, namely a flat mode and a first harmonic are necessarily symmetric, hence, with no loss of generality, for such initial data we may take the symmetry axis to be at  $x = 0$ , and thus the projection of such solutions to the  $(q, p)$  plane utilizing the cosine transform  $C_1$  (centred at the origin) is natural.
5. We expect that in the two-mode zone, namely when  $I(t) < I_{2\text{LUM}}$  and the initial data have sufficiently fast decay of the high modes, the ODE and the PDE systems will behave similarly. Indeed, we demonstrate below that all the near-integrable ODE behaviours appear in the PDE as well. When solutions that are initialized in this zone leave it, possibly by two d.o.f. instability mechanisms that ramp  $I$  beyond the  $I_{2\text{LUM}}$  threshold, other modes of the solution become active and, as explained in section 3.3, intermittent spatial-temporal chaos emerges.

*Regular solutions.* Solutions with initial profiles that are bounded away from the unstable branch of the plane wave and its homoclinic orbits and satisfy  $I(0) < I_{2\text{LUM}}$  are observed to execute, for sufficiently small  $\varepsilon$  (e.g. for  $\varepsilon \approx 10^{-3}$  for the initial conditions shown in figure 10), quasi-periodic motion (up to the numerical accuracy). Note that the solutions that appear in figure 10 are far from the quiescent solution, namely, they have a finite power. In fact, figure 10 shows KAM like solutions with  $I > I_{1\text{LUM}}$ , demonstrating that away from the unstable branches of the special solutions, the perturbed PDE phase space may indeed have many regular orbits. We conclude that an infinite-dimensional KAM theorem may hold here even for large amplitude solutions (see [22] for related rigorous results in the small amplitude regime).

The projection  $\zeta_t$  of such regular non-resonant orbits (respectively, resonant) to the PDE-EMBDs appears as an ordered covering of a confined rectangular region of width  $O(\varepsilon)$  and height  $O(\varepsilon)$  (respectively  $O(\sqrt{\varepsilon})$ ).

The projection of the non-resonant regular perturbed solution onto the phase-power plane appears as a band of height  $O(\varepsilon)$  around  $I(\Psi_0(x))$  that covers uniformly all values of  $\gamma$  (yet  $\gamma(t)$  may be non-monotone), similar to the corresponding unperturbed trajectories. Resonant regular quasi-periodic motion projects to the phase-power plane as a band of height  $O(\sqrt{\varepsilon})$  that is distinct from the projection of the integrable solutions, and, in particular it is non-uniform in  $\gamma$ . The projection to the  $qp$ -plane of both the unperturbed and perturbed solutions is non-trivial as the true second mode is composed of many Fourier components. Nonetheless, it provides information regarding exterior and interior type of dynamics.

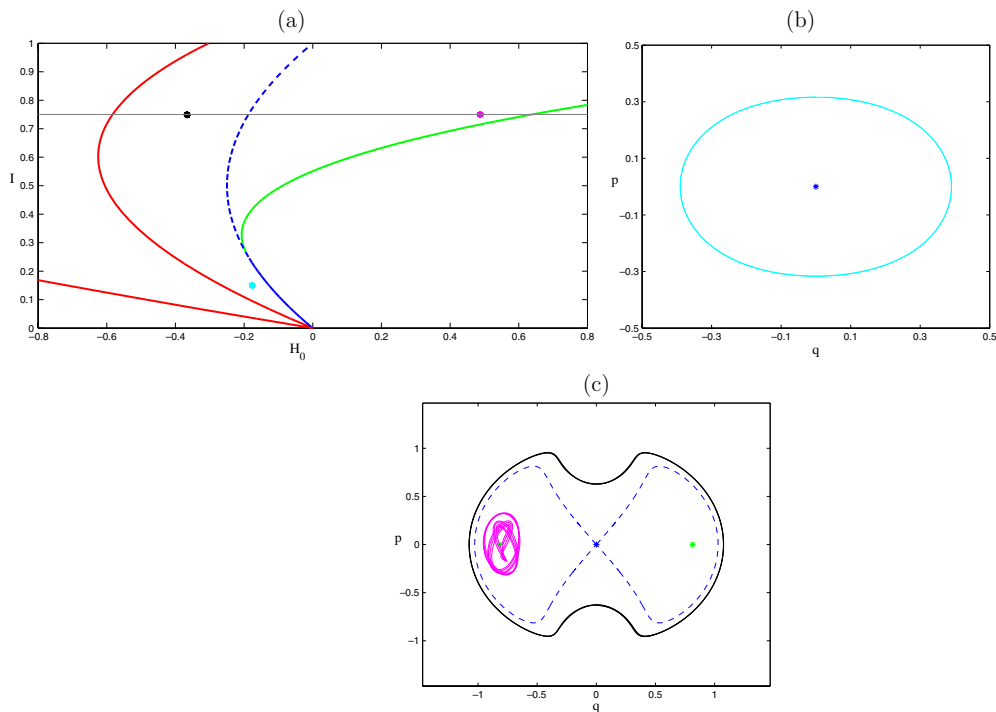


**Figure 10.** Three perturbed regular PDE solutions. The magenta/black/cyan orbits are the P1 (a) and P3 (b), (c) projections of the near-integrable regular interior/exterior/elliptic solutions (with  $\varepsilon = 10^{-3}$ ,  $k = 1$ ,  $\Omega^2 = 1$ ,  $g = 2$ ). Some of the integrable solutions (blue—the plane wave and its homoclinic orbits, green—the inner solution with multiplicity 1, red—the outer solutions) are shown. (a) The PDE-EMBD for  $I < I_{2LUM}$ , with the three P1 projections of the solutions. (b) P3-projection (to the  $qp$ -plane) of an elliptic solution with initial data  $\Psi_0(x) = [\frac{\sqrt{0.1}}{\sqrt{2}} + \sqrt{0.1} \cos(kx)]e^{iy(0)}$  (so  $I(t = 0) = 0.15$ ). The origin (blue point) is the P3-projection of the stable plane wave at  $I = 0.15$ . (c) P3-projection of the exterior ( $\Psi_0(x) = [\frac{\sqrt{1.1}}{\sqrt{2}}|c| + \sqrt{0.4i} \cos(kx)]e^{iy(0)}$ ) and interior ( $\Psi_0(x) = [\frac{\sqrt{0.9}}{\sqrt{2}}|c| - \sqrt{0.6} \cos(kx)]e^{iy(0)}$ ) solutions at  $I(t = 0) = 0.75$  (the horizontal line in the PDE-EMBD). The dashed blue curves (respectively green points) are the P3-projections of the symmetric unperturbed homoclinic orbits (of the symmetric unperturbed inner-dnoidal solutions with multiplicity 1).

We can now classify the typical PDE quasi-periodic motion near the plane waves to four classes of solutions that are similar to the ODE classes. Yet, the classification here is non-rigorous (in particular, note that in the ODE case each point on the EMBD corresponds to a unique level set of the integrable motion, whereas the PDE-EMBD does not preserve this property). Thus, we present numerical evidence for its validity for the two-mode initial data of the form (3.11) that was considered in theorem 6. We emphasize that here only the initial data are taken in the truncated form—the forced NLS equations are integrated with an 8th order finite-difference in space and 4th order Runge–Kutta in time scheme (similar results appear when a spectral code with 512 modes is utilized), and for all  $t > 0$  we do observe that some small power is spread to the higher Fourier modes.

*Non-resonant elliptic solutions.* Solutions with initial profiles (3.11) satisfying  $I(\Psi_0(x)) < I_{1LUM}$  are typically, for sufficiently small  $\varepsilon$ , quasi-periodic and remain  $\varepsilon$ -close to a nearby integrable solution. Their projection to the PDE-EMBD lies to the left of the plane wave SSC

curve (see figure 10(a) and theorem 6). Their projection to the  $qp$ -plane,  $\xi_t$ , results with orbits encircling the origin, see figure 10(b). Their projection  $\rho_t$  onto the phase–power plane appears as  $\varepsilon$ -deformed horizontal lines (not shown).

*Non-resonant exterior solutions.* Similarly, for most initial profiles of the form (3.11) satisfying  $\text{Re}[b(0)] = 0$ ,  $\text{Im}[b(0)] \neq 0$  and  $I(\Psi_0(x)) \in (I_{\text{ILUM}}, I_{\text{2LUM}})$ , the perturbed solutions are quasi-periodic and remain  $\varepsilon$ -close to an exterior integrable solution oscillating around the outer-cnoidal like solutions (figure 10(c)). Their projection onto the PDE-EMBD is to the left of the plane wave SSC, see figure 10(a) and theorem 6.

*Non-resonant interior solutions.* Solutions with initial profiles of the form (3.11) satisfying  $\text{Re}[b(0)] \neq 0$ ,  $\text{Im}[b(0)] = 0$  and  $I(\Psi_0(x)) \in (I_{\text{ILUM}}, I_{\text{2LUM}})$  are typically quasi-periodic and remain  $\varepsilon$ -close to an integrable solution which oscillates about the inner-dnoidal standing wave in the interior of the homoclinic orbit, see figure 10(c). The sign of  $\text{Re}[b(0)]$  determines whether the solution oscillated about the right ( $\text{Re}[b(0)] > 0$ ) or left ( $\text{Re}[b(0)] < 0$ ) dnoidal standing wave. In contrast to the two d.o.f case, the projected interior integrable orbits to the  $qp$ -plane may have a complicated shape, see figure 10(c). The projection of such perturbed solutions onto the PDE-EMBD is to the right of the plane wave SSC, see figure 10(a) and theorem 6.

*Resonant solutions.* Resonant elliptic, interior and exterior solutions appear for a ‘small fraction’ of the above listed initial profiles<sup>12</sup>. Their projections onto the PDE-EMBD and the  $qp$ -plane, extends to variation of  $\mathcal{O}(\sqrt{\varepsilon})$  in  $I$ . Their projection to the  $(\gamma, I)$  plane, in the rotational resonant frame, is pendulum-like. The strongest resonances, namely those that appear at the folds of the different SSC in the PDE-EMBD (theorem 5), produce the largest resonance zones. In particular, if  $\Omega^2 < \Omega_{\text{PR}}^2$ , then the plane wave SSC has a fold at  $I_{\text{pw-res}} < I_{\text{ILUM}}$  and thus, for most initial profiles  $\Psi_0(x)$  in the rectangle of height  $\mathcal{O}(\sqrt{\varepsilon})$  near this fold (with  $\varepsilon$  sufficiently small so that  $\sqrt{\varepsilon} \ll (I_{\text{ILUM}} - I_{\text{pw-res}})$ ) the perturbed solutions are resonant yet regular. Their projection onto the phase–power plane is pendulum-like and these are easily observable even for  $\varepsilon \approx 10^{-3}$ . See figure 1(a) in [53] for such trajectories in the case of relatively large  $\varepsilon$ , where the resonant zone exceeds the  $I_{\text{ILUM}}$  bound.

*Temporally chaotic solutions.* Perturbed solutions that visit the neighbourhood of the plane wave in its unstable regime ( $I \in (I_{\text{ILUM}}, I_{\text{2LUM}})$ ) yet do not invade the region  $I > I_{\text{2LUM}}$  exhibit temporal chaos that follow closely the two d.o.f orbits. As in the two d.o.f case, three observable chaotic scenarios arise, and their projections P1–P3 to the three planes—the PDE-EMBD, the  $(\gamma, I)$  plane and the  $(q, p)$  plane follow closely those of the ODE;

*Homoclinic chaos.* Given a  $\delta > 0$ , for sufficiently small  $\varepsilon$ , solutions with initial profiles of the form (3.11) satisfying  $0 < |b(0)| = \mathcal{O}(\varepsilon)$  and  $I(\Psi_0(x)) \in (I_{\text{ILUM}}, I_{\text{2LUM}}) \setminus [I_{\text{pw-res}} - \delta, I_{\text{pw-res}} + \delta]$ , will typically exhibits homoclinic chaos. Such initial profiles project onto the PDE-EMBD in an  $\mathcal{O}(\varepsilon)$  neighbourhood of the SSC in the interior of the interval  $(I_{\text{ILUM}}, I_{\text{2LUM}})$ , at a point which is bounded away from the resonant plane wave solution, the SSC extrema point  $I_{\text{pw-res}} = \Omega^2/g$  ( $= 0.4$  in figure 11(HC)). The projected curve is composed of nearly horizontal lines (corresponding to the homoclinic excursions along which  $I$  changes by  $\mathcal{O}(\varepsilon)$ ) and occasional crossing of the SSC curve (see figure 11).

*Hyperbolic resonance.* For  $\Omega^2 \in (k^2/2, 2k^2)$ , for sufficiently small  $\varepsilon$ , solutions with initial profiles of the form (3.11) satisfying  $0 < |b(0)| = \mathcal{O}(\varepsilon)$  and

<sup>12</sup> The initial profile (3.11) depends on four real parameters,  $\{|c|, \gamma(0), \text{Re}[b(0)], \text{Im}[b(0)]\}$ , and since we take  $I < I_{\text{2LUM}}$  these parameters belong to a bounded domain. Thus the notion of typical initial condition of this family may be precisely defined.

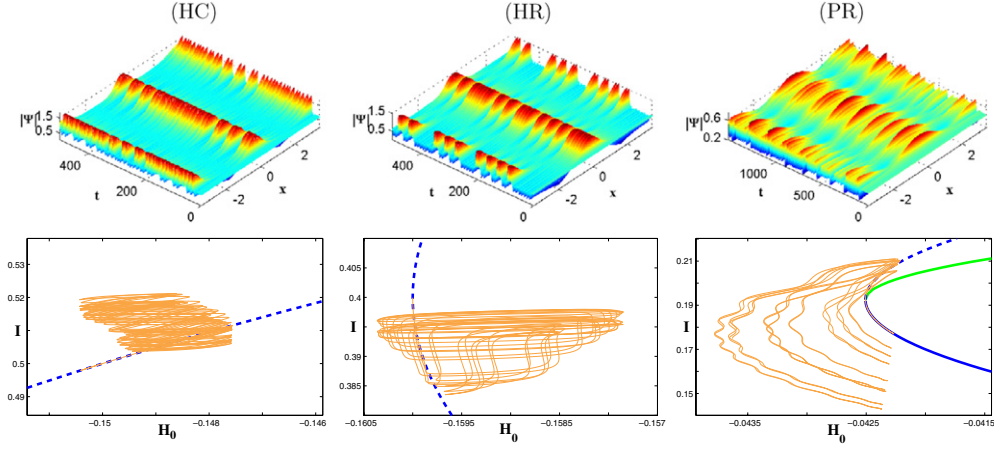


**Figure 11.** Three different types of temporal chaos in the forced NLS equation. The periodic length is fixed to  $k = 2\pi/L = 0.9$  and the initial profile is near the unstable plane wave:  $\Psi_0 = \sqrt{A}e^{i\gamma_0} + 10^{-5} \cos kx$ ,  $\varepsilon = 10^{-3}$ , with the values (HC) Homoclinic chaos:  $\Omega^2 = 0.8$ ,  $A = 0.5$ ,  $\gamma_0 = 1/4\pi$  (HR) Hyperbolic resonance:  $\Omega^2 = 0.8$ ,  $A = 0.4$ ,  $\gamma_0 = 1/4\pi$  and (PR) Parabolic resonance:  $\Omega^2 = 0.405$ ,  $A = 0.2$ ,  $\gamma_0 = 3/4\pi$ .

$I(\Psi_0(x)) \in [I_{\text{pw-res}} - \mathcal{O}(\sqrt{\varepsilon}), I_{\text{pw-res}} + \mathcal{O}(\sqrt{\varepsilon})]$ , typically exhibit hyperbolic resonance chaos. The initial profile projects onto the PDE-EMBD in a rectangle of height  $\mathcal{O}(\sqrt{\varepsilon})$  that crosses the SSC in the interior of the interval  $(I_{1\text{LUM}}, I_{2\text{LUM}})$  near the SSC extremal point  $I_{\text{pw-res}}$ , see figure 11(HR). The projected curve is composed, as in the truncated case, from almost horizontal lines (homoclinic excursions) and abrupt  $\mathcal{O}(\sqrt{\varepsilon})$  excursions in  $I$  that correspond to some shadowing of the resonance zone dynamics (see [32, 38] for related analysis).

*Parabolic resonance.* Near the critical parameters' values  $\Omega^2 \approx \Omega_{\text{PR}}^2 = (k^2/2)$  (where  $I_{\text{pw-res}} \approx I_{1\text{LUM}}$ ), for sufficiently small  $\varepsilon$ , solutions with initial profiles of the form (3.11) satisfying  $0 < |b(0)| = \mathcal{O}(\varepsilon)$  and  $I(\Psi_0(x)) \in [I_{\text{pw-res}} - \mathcal{O}(\sqrt{\varepsilon}), I_{\text{pw-res}} + \mathcal{O}(\sqrt{\varepsilon})]$ , typically exhibit the parabolic-resonance chaos, see figure 11(PR). The shape and form of these parabolic resonant solutions are similar to that of the parabolic resonant solutions of the truncated system as long as  $I(t) < I_{2\text{LUM}}$  [52]. This latter condition is satisfied in the limit of sufficiently small  $\varepsilon$ . In section 3.3 we show that these solutions actually follow the level lines of an adiabatic invariant of a simplified two d.o.f. normal form, thus finding the scaling for the observed intermittent chaotic motion.

*Spatio-temporal chaotic solutions.* When solutions are either initialized or evolve to the region near the plane wave with  $I > I_{2\text{LUM}}$ , spatio-temporal dynamics arise. Then, at least two spatially non-trivial modes evolve chaotically in time, typically with chaotic relative phase, and thus their spatial profile becomes uncorrelated [18, 53]. Since the perturbed system preserves the space of spatially symmetric functions (see [17]), such a behaviour is possible only when asymmetric initial data are introduced (yet, we find that even the slightest asymmetry in the initial data or in the numerical code is sufficient to induce the appearance of STC when  $I(t) > I_{2\text{LUM}}$ ). We can thus conclude that if a typical (asymmetric) solution projection to the PDE-EMBD crosses the  $I = I_{2\text{LUM}}$  line near the plane wave SSC,

it exhibits STC<sup>13</sup>. Auto-correlation plots, amplitude plots or even Fourier mode phase plots support this observation [53]. Can a nearly quiescent initial profile (with small  $I(0)$ ) evolve to reach the temporal-chaos region (with  $I(t) > I_{1\text{LUM}}$ ) or even the spatial-temporal region ( $I(t) > I_{2\text{LUM}}$ )? We propose that for sufficiently small  $\varepsilon$  the answer is negative: the numerical indications are that for small  $\varepsilon$  the nearly quiescent solutions of the forced NLS behave as the solutions of the truncated model, where, by KAM theory, they cannot increase their initial power by more than  $\mathcal{O}(\sqrt{\varepsilon})$  and thus remain forever in the small  $I$  region (for the forced NLS—these are finite-time numerical results).

On the other hand, for sufficiently *large*  $\varepsilon$  it is always possible to ramp  $I$  up to  $I_{2\text{LUM}}$  on a time scale of order  $\mathcal{O}(1/\sqrt{\varepsilon})$  by the plane wave resonance mechanism; Indeed, note that on this flat invariant plane the dynamics is governed by the Hamiltonian (3.8). Indeed, equation (3.9) implies that when  $\Delta\bar{I} \gtrsim \bar{I}^{\text{res}}$  nearly quiescent solutions are swept into the resonances zone. Hence, for any given  $\Omega$ , there is a critical  $\varepsilon_0(\Omega)$ :

$$\varepsilon_0(\Omega) = \frac{\Omega^3}{4\sqrt{g}} \quad (3.12)$$

beyond which the resonance zone extends from the origin to  $\bar{I}^{\text{res}} + \Delta\bar{I}$ . Similarly, this resonance zone extends beyond  $I_{2\text{LUM}}$  when  $\bar{I}^{\text{res}} + \Delta\bar{I} \gtrsim I_{2\text{LUM}}$ , and another critical value,  $\varepsilon_{2\text{LUM}}(\Omega, k)$ , emerges:

$$\varepsilon_{2\text{LUM}}(\Omega, k) = \frac{1}{\Omega\sqrt{g}} \left( k^2 - \frac{\Omega^2}{2} \right)^2. \quad (3.13)$$

Thus, for  $\varepsilon > \varepsilon_{c\text{-flat}}(\Omega, k) = \max\{\varepsilon_0(\Omega), \varepsilon_{2\text{LUM}}(\Omega, k)\}$ , the  $L_2$  norm of typical nearly quiescent *flat* solutions is ramped up beyond  $I_{2\text{LUM}}$ . Note that  $\varepsilon_{c\text{-flat}}(\Omega, k)$  is minimal at  $\Omega^2 = k^2$ . For example, for the parameters  $(g, k)$  that are chosen in [53],  $k = 0.9$  and  $g = 2$ ,  $\varepsilon_{c\text{-flat}}(0.9, 0.9) = \frac{(0.9)^3}{4\sqrt{2}} \approx 0.129$ . Non-flat nearly quiescent initial data evolve to STC when  $\varepsilon > \varepsilon_c(\Omega, k)$ , where clearly  $\varepsilon_c(\Omega, k) \leq \varepsilon_{c\text{-flat}}(\Omega, k)$ . In [53] we find numerically that  $\varepsilon_c(\Omega, k)$  is actually minimal at parabolic resonance (namely the minimum shifts to  $\Omega^2 = k^2/2$ ) and that  $\varepsilon_c(\frac{0.9}{\sqrt{2}}, 0.9) \approx 0.05$ .

### 3.3. The parabolic-resonance phenomena

The appearance of parabolic resonance in the truncated two d.o.f system (equation (3.6)) may be fully analysed by transforming the truncated model into the symmetric parabolic-resonance normal form that has recently been constructed and analysed [50]. We provide the transformation to the normal form below and show that for small  $\varepsilon$  the projection of the PDE solution onto the first two Fourier modes (projections P2, P3 to  $(x^p(t), y^p(t), I^p(t), \gamma^p(t))$ ) follow the same adiabatic invariants as the two d.o.f model.

To analyse the truncated system, we introduce below a change of coordinates that brings the truncated model, in the leading order term, to the parabolic-resonance slow-fast normal form:

$$\begin{aligned} \bar{H}(q, p, \bar{I}, \gamma; g, k, \Omega^2, \varepsilon) &\rightarrow \varepsilon^{\text{nf}} [H^{\text{nf}}(q^{\text{nf}}, p^{\text{nf}}, I^{\text{nf}}, \varphi^{\text{nf}}; \beta, \lambda) \\ &+ (\varepsilon^{\text{nf}})^{\frac{1}{2}} H_p(q^{\text{nf}}, p^{\text{nf}}, I^{\text{nf}}, \varphi^{\text{nf}}; \varepsilon^{\text{nf}})], \end{aligned}$$

<sup>13</sup> So far, there is no indication that such solutions may lead to weak turbulence: it appears that even-though the dynamics are chaotic and involve several modes, the energy remains concentrated only in the lowest Fourier modes (see [18, 53] and figures therein).

where (hereafter we drop the nf superscripts when unambiguous)

$$H^{\text{nf}}(q, p, I, \varphi) = \frac{p^2}{2} - I \frac{q^2}{2} + \frac{q^4}{4} + \beta \frac{(\lambda + I)^2}{2} + \cos \varphi \quad (3.14)$$

is equipped with the slow-fast symplectic form  $dq \wedge dp + \varepsilon^{-1/4}(d\varphi \wedge dI)$  so that the velocities in the fast  $(q, p)$  variables are of  $O(1)$  and those in the slow  $(I, \varphi)$  variables are of  $O(\varepsilon^{1/4})$ .

Most importantly, the parameters  $\lambda, \beta, \varepsilon$  that appear in the normal form are

$$\lambda = \frac{128}{49\sqrt{\varepsilon^{\text{nf}}}} \left( \frac{1}{2} - \frac{\Omega^2}{k^2} \right), \quad \beta = -\frac{7}{16}, \quad \varepsilon^{\text{nf}} = \frac{4^5 \sqrt{2g}}{7^3 k^3} \varepsilon \approx \frac{4.22 \sqrt{g}}{k^3} \varepsilon \quad (3.15)$$

Note, in particular, that  $\beta$  is independent of the forced NLS parameters, that  $\lambda$  is tunable by changing  $\Omega$  and that  $\varepsilon^{\text{nf}}$  has non-trivial dependence on  $k$ .

The transformation to the normal form is given by (with  $a = (\sqrt{7}k/4\sqrt{g})$ ,  $b = 2(\frac{\sqrt{7}}{4})^3 \frac{k}{\sqrt{g}}$ ):

$$q = a\sqrt{\varepsilon^{\text{nf}}} q^{\text{nf}}, \quad p = b\sqrt{\varepsilon^{\text{nf}}} p^{\text{nf}}, \quad \bar{I} = ab\sqrt{\varepsilon^{\text{nf}}} I^{\text{nf}} + \frac{1}{2}k^2, \quad \gamma = \varphi^{\text{nf}} - \pi/2$$

$$\bar{H} = -k^2 b^2 \varepsilon^{\text{nf}} H^{\text{nf}} - \frac{\Omega^4}{2g}, \quad \bar{t} = -\frac{t^{\text{nf}}}{\sqrt[4]{\varepsilon^{\text{nf}}} k^2 b^2}.$$

So that the perturbation near the parabolic-resonance region becomes

$$\begin{aligned} \sqrt{\varepsilon^{\text{nf}}} H_p(q^{\text{nf}}, p^{\text{nf}}, I^{\text{nf}}, \varphi^{\text{nf}}; \varepsilon^{\text{nf}}) &= \sqrt{\varepsilon^{\text{nf}}} \frac{3}{8} \frac{7}{16} (q^{\text{nf}})^2 (p^{\text{nf}})^2 - \varepsilon^{\text{nf}} \frac{7^3}{4^7} (p^{\text{nf}})^4 \\ &+ \left( \sqrt{1 + \frac{7}{16} \sqrt{\varepsilon^{\text{nf}}} \left( \frac{7}{4} I^{\text{nf}} - (q^{\text{nf}})^2 \right)} - \varepsilon^{\text{nf}} \frac{7^3}{4^5} (p^{\text{nf}})^2 - 1 \right) \cos \varphi \\ &= \sqrt{\varepsilon^{\text{nf}}} \left( \frac{3}{8} \frac{7}{16} (q^{\text{nf}})^2 (p^{\text{nf}})^2 + \frac{7}{32} \left( \frac{7}{4} I^{\text{nf}} - (q^{\text{nf}})^2 \right) \cos \varphi \right) + O(\varepsilon^{\text{nf}}). \end{aligned}$$

Note that for any fixed  $(I, \varphi)$  the Hamiltonian  $H^{\text{nf}}(q, p, I, \varphi; \beta, \lambda)$  corresponds to the classical Duffing oscillator; for negative  $I$  this Hamiltonian has a single stable fixed point at the origin, whereas for positive  $I$  the system has a figure eight separatrix emanating from the origin with two elliptic fixed points at  $(q, p) = (\pm\sqrt{I}, 0)$ . The motion in the  $(q, p)$  plane is fast as long as the  $qp$  orbit is bounded away from the separatrix. Thus, on each energy surface  $H^{\text{nf}}(\cdot) = h$ , we define the separatrix set  $S_{qp}(h)$  as the set of  $(I, \varphi)$  values that correspond to the  $(q, p)$  separatrix level set

$$S_{qp}(h) = \left\{ (I, \varphi) \mid I > 0 \text{ and } h = H^{\text{nf}}(0, 0, I, \varphi) = \beta \frac{(\lambda + I)^2}{2} + \cos \varphi \right\}. \quad (3.16)$$

It follows that for values of  $(I, \varphi)$  that are bounded away from  $S_{qp}(h)$  the motion in the  $(q, p)$  plane is fast, and hence, by the adiabatic theorem, it preserves an adiabatic invariant [50]. To first order in  $\varepsilon^{1/4}$ , the adiabatic invariant is given by the  $qp$ -area that is enclosed by the fast trajectories, namely the action  $J(I, \varphi; h)$ :

$$J(I, \varphi; h) = 2 \int_{q_-}^{q_+} p \, dq = 2\sqrt{2} \int_{q_-}^{q_+} \sqrt{z(\varphi; h) + \frac{q^2}{2} - \frac{q^4}{4} - \beta \frac{(\lambda + I)^2}{2}} \, dq, \quad (3.17)$$

$$z(\varphi; h) = h - \cos \varphi, \quad (3.18)$$

where  $q_+$  and  $q_-$  are properly defined to make  $J(I, \varphi; h)$  continuous across the separatrix set. The perturbed motion projected to the  $(I, \varphi)$  plane follows the level lines of  $J(I, \varphi; h)$  up to

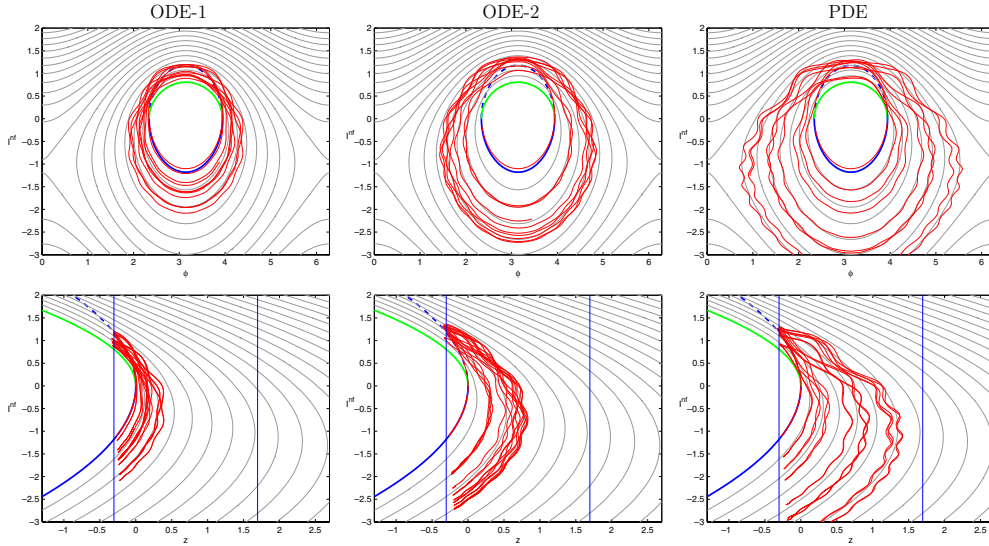


**Figure 12.** Adiabatic chaos in the forced NLS. Trajectories of the forced truncated model equation (ODE-1, ODE-2 columns) and of the forced NLS PDE (PDE column) with initial conditions near the plane wave solution are projected (red) on top of the level sets of the adiabatic invariant of the normal form  $J(I, \varphi; h)$ . The sets corresponding to the stable plane wave  $(S_{qp} \Big|_{\{I^{nf} < 0, (q, p) = (0, 0)\}})$  and ground state  $(S_{qp} \Big|_{\{I^{nf} > 0, (q, p) = (\pm\sqrt{I^{nf}}, 0)\}})$  circles and are marked by solid blue and green curves, respectively, and the separatrix set  $(S_{qp} \Big|_{\{I^{nf} > 0, (q, p) = (0, 0)\}})$  is indicated by a dashed blue curve. First row: the trajectories are projected to the  $(\varphi^{nf}, I^{nf})$  plane. Second row: the trajectories are projected to the  $(z, I^{nf})$  plane. The vertical lines show the energy surface boundaries. In all figures  $h = 0.695$ ,  $\varepsilon = 10^{-3}$ . The initial conditions for ODE-1 and PDE are:  $(q, p, I, \varphi) = (10^{-5}, 0, 0.2, \frac{5}{4}\pi)$ , for ODE-2 the initial conditions are  $(x, y, I, \varphi) = (5 \times 10^{-5}, 0, 0.2, \frac{5}{4}\pi)$ .

the separatrix set, where it undergoes a jump. This quasi-regular behaviour is called adiabatic chaos: such a behaviour has been extensively studied theoretically and in the context of various applications [7, 19, 27, 46, 47, 56].

The level lines of  $J(I, \varphi; h)$  change their shape and even their topology for different energies, thus a full description of the dynamics for all energies appears to be formidable. However, since  $J(I, \varphi; h) = J(z(\varphi; h), I)$  and since the dependence of  $z$  on  $\varphi$  and  $h$  is so simple to decipher (see equation (3.18)), projecting the  $J$  level lines to the  $(z, I)$  plane provides a full description of the perturbed dynamics at any energy level; Up to the  $\sqrt{\varepsilon}H_p$  corrections, the perturbed motion at the energy level  $h$  is confined to the strip  $z \in [h - 1, h + 1]$ , and thus occurs along the  $J$  level lines in that strip. The separatrix set projection to the  $(z, I)$  plane is simply the upper part of the parabola  $\beta((\lambda + I)^2/2)$  (see equation (3.16)). Hence, at any energy, the  $J$  level lines that intersect the separatrix set in the strip  $z \in [h - 1, h + 1]$  correspond exactly to the chaotic set.

In figure 12 trajectories of the forced truncated model equation (marked as ODE-1, ODE-2) and of the forced NLS (marked as PDE) transformed to the normal form coordinate system are shown. These trajectories (red) are compared with the level sets of the adiabatic invariant  $J(I, \varphi; h)$  (grey) of the normal form system in the  $(I, \varphi)$  plane (first row) and in the  $(z, I)$  plane (second row). It is clearly observed that both the PDE and the ODE perturbed trajectories

follow the level sets of the adiabatic invariant except near the separatrix set (dashed blue line). In the second row of figure 12 the trajectories are projected to the  $(z, I)$  plane, where the energy surface bounds on  $z$  are shown. We observe numerically that the adiabatic invariant is preserved away from the separatrices for  $\varepsilon^{\text{nf}} \lesssim 0.001$ . For such values, the region of chaotic behaviour is of order  $\sqrt{\varepsilon^{\text{nf}}}$ , and thus, in particular the instability in  $I$  values is limited to  $O(\sqrt{\varepsilon^{\text{nf}}})$ . Notably, for  $k = 0.9$ ,  $g = 2$  we get  $\varepsilon^{\text{nf}} = 8.19\varepsilon$ . The critical value of  $\varepsilon_c = 0.05$  that was found numerically to produce the transition of nearly quiescent initial data to STC solutions in [53] corresponds to  $\varepsilon^{\text{nf}} = 0.41$ , where the leading order adiabatic chaos analysis is clearly invalid.

#### 4. Conclusions and discussion

By constructing the PDE-EMBD, we show that the standing and the travelling waves solutions of the periodic one-dimensional NLS equation may serve as organizing skeleton for the PDE phase-space structure near these special solutions. We find that these families of solutions project as distinct curves (called SSC) in the PDE-EMBD. We proved that the folds of these curves correspond to resonances of the standing/travelling waves solutions. We completed the PDE-EMBD by including the information regarding the stability of the three families of the standing waves. We provided a modified proof for the linear instability of the inner standing waves solutions with multiplicity  $j \geq 2$ . We studied the linear stability of the outer standing waves solutions numerically and found that these waves undergo a sequence of Hamiltonian–Hopf bifurcations. The Hopf bifurcations appear at  $I_{\text{bif}}^m(\Phi_j^{\text{out}}(x)) = (m^2/g)k^2$ , with similar scaling to that of the plane wave modulation instability. A proof of this numerical result should complete the rigorous study of linear stability/instability of all the standing waves solutions in the one-dimensional periodic NLS. The stability analysis of the travelling wave solutions is still open.

The PDE-EMBD provides a convenient way to classify the solutions of the perturbed problem near the SSCs. In an  $O(\varepsilon)$ -neighbourhood of unstable branches of the SSC, one expects to find chaotic solutions, whereas away from such branches, infinite-dimensional KAM type solutions are expected to arise. Near folds of the SSC resonances are created. We use these observations to classify the type of solutions that appear near the plane wave, thus providing a phase-space analysis for the PDE in the SSC neighbourhood.

For a stable KAM like solution, all constants of motion must remain in an  $O(\varepsilon)$  neighbourhood of their initial value, and thus it projects to an  $\varepsilon$ -square in the PDE-EMBD that is typically bounded away from any unstable SSC, see figure 10. Notably, such a solution must be bounded away from all other families of degenerate unstable solutions of the integrable NLS. While the PDE-EMBD that includes both the standing and the travelling waves of many multiplicities is already rather complicated to grasp (figure 7), the full diagram should include the bifurcating modes from the Hamiltonian–Hopf bifurcations and other finite-dimensional quasi-periodic solutions of the integrable system. Gaps in such a diagram may indicate the stability region in which KAM like solutions reign.

When  $\Omega^2 \approx k^2/2$  the plane wave solution has an amplitude at which it is both resonant and parabolic. In [51, 52] we showed that perturbed solutions that are initialized near the plane wave exhibit instabilities that are similar to those arising in the truncated NLS equation. Here we showed that the emerging parabolic-resonance mechanism in the truncated model may be analysed by the adiabatic-chaos methodology. In particular, we showed that there exists an adiabatic invariant that is approximately preserved away from the separatrix set. We showed that the PDE solutions also preserve the same invariant as long as their  $L_2$  norm does not

exceed  $2k^2/g$ . We observed that the transition to STC that was reported in [53] appears at  $\varepsilon$  values for which the leading order approximation of the adiabatic invariant level lines is not followed. Since the PDE and the truncated model solutions exhibit similar behaviour at these  $\varepsilon$  values, we believe that higher order approximation of the adiabatic invariant may explain this phenomena.

We have provided a phase-space description of the PDE solutions near the plane wave when it has a limited power. Clearly, the classification of perturbed motion for general initial data is far from being complete. Other chaotic mechanisms, for example, near the newly discovered Hopf bifurcations of the unperturbed outer solutions, are yet to be studied.

## Acknowledgments

The authors acknowledge the support of Israel Science Foundation (Grant 273/07), Minerva foundation and Russian-Israeli joint grant (MNTI-RFBR No 06-01-72023). They also thank J Gibbon, A Soffer, E Titi, D Turaev and M Weinstein for stimulating discussions.

## References

- [1] Ablowitz M and Segur H 1981 *Solitons and the Inverse Scattering Transform* (PA: SIAM)
- [2] Agrawal G 2001 *Nonlinear Fiber Optics* (New York: Academic)
- [3] Akhmediev N N and Ankiewicz A 1997 *Solitons : nonlinear pulses and beams / Nail N. Akhmediev and Adrian Ankiewicz* (London: Chapman and Hall)
- [4] Pava J A, Bona J L and Scialom M 2006 Stability of cnoidal waves *Adv. Diff. Eqns* **11** 1321–74
- [5] Pava J A and Natali F M A 2008 Positivity properties of the Fourier transform and the stability of periodic traveling-wave solutions *SIAM J. Math. Anal.* **40** 1123–51
- [6] Pava J A 2007 Nonlinear stability of periodic traveling wave solutions to the Schrödinger and the modified Korteweg–de Vries equations *J. Diff. Eqns* **235** 1–30
- [7] Arnol'd V I 1993 *Dynamical Systems III (Encyclopedia of Mathematical Sciences vol 3)* 2nd edn (Berlin: Springer)
- [8] Brooke Benjamin T and Feir J E 1967 The disintegration of wave trains on deep water: I. Theory *J. Fluid Mech. Digital Arch.* **27** 417–30
- [9] Benjamin T B 1972 The stability of solitary waves *Proc. R. Soc. Lond. Ser. A* **328** 153–83
- [10] Bishop A R, Flesch R, Forest M G, McLaughlin D W and Overman II E A 1990 Correlations between chaos in a perturbed Sine-Gordon equation and a truncated model system *SIAM J. Math. Anal.* **21** 1511–36
- [11] Bishop A R, Forest M G, McLaughlin D W and Overman II E A 1986 A quasi-periodic route to chaos in a near-integrable PDE *Physica D* **23** 293–328
- [12] Bishop A R, Forest M G, McLaughlin D W and Overman II E A 1990 A modal representation of chaotic attractors for the driven, damped pendulum chain *Phys. Lett. A* **144** 17–25
- [13] Bishop A R, Fesser K, Lomdahl P S, Kerr W C, Williams M B and Trullinger S E 1983 Coherent spatial structure versus time chaos in a perturbed sine-Gordon system *Phys. Rev. Lett.* **50** 1095–8
- [14] Bishop A R and Lomdahl P S 1986 Nonlinear dynamics in driven, damped sine-Gordon systems *Physica D* **18** 54–66
- [15] Bishop A, McLaughlin D W, Forest M G and Overman E II 1988 Quasi-periodic route to chaos in a near-integrable PDE: homoclinic crossings *Phys. Lett. A* **127** 335–40
- [16] Bona J 1975 On the stability theory of solitary waves *Proc. R. Soc. Lond. Ser. A* **344** 363–74
- [17] Cai D, McLaughlin D W and McLaughlin K T R 2002 The nonlinear Schrödinger equation as both a PDE and a dynamical system *Handbook of Dynamical Systems* vol 2 (Amsterdam: North-Holland) pp 599–675
- [18] Cai D, McLaughlin D W and Shatah J 1999 Spatiotemporal chaos and effective stochastic dynamics for a near-integrable nonlinear system *Phys. Lett. A* **253** 280–6
- [19] Cary J R and Skodje R T 1989 Phase change between separatrix crossings *Physica D* **36** 287–316
- [20] Cushman R H and Bates L M 1997 *Global Aspects of Classical Integrable Systems* (Basle: Birkhauser)

- [21] Davis K B, Mewes M O, Andrews M R, van Druten N J, Durfee D S, Kurn D M and Ketterle W 1995 Bose-Einstein condensation in a gas of sodium atoms *Phys. Rev. Lett.* **75** 3969–73
- [22] Eliasson L H and Kuksin S B 2010 KAM for the nonlinear Schrödinger equation *Ann. Math.* **172** (1) 371–435
- [23] Ercolani N, Forest M G and McLaughlin D W 1990 Geometry of the modulational instability: III. Homoclinic orbits for the periodic sine-Gordon equation *Physica D* **43** 349–84
- [24] Gally T and Hărăguș M 2007 Orbital stability of periodic waves for the nonlinear Schrödinger equation *J. Dyn. Diff. Eqns* **19** 825–65
- [25] Gally T and Hărăguș M 2007 Stability of small periodic waves for the nonlinear Schrödinger equation *J. Diff. Eqns* **234** 544–81
- [26] Geng J and You J 2005 A KAM theorem for one dimensional Schrödinger equation with periodic boundary conditions *J. Diff. Eqns* **209** 1–56
- [27] Gorelyshev I and Neishtadt A 2008 Jump in adiabatic invariant at a transition between modes of motion for systems with impacts *Nonlinearity* **21** 661–76
- [28] Grillakis M, Shatah J and Strauss W 1987 Stability theory of solitary waves in the presence of symmetry: I *J. Funct. Anal.* **74** 160–97
- [29] Grillakis M, Shatah J and Strauss W 1990 Stability theory of solitary waves in the presence of symmetry: II *J. Funct. Anal.* **94** 308–48
- [30] Grillakis M 1988 Linearized instability for nonlinear Schrödinger and Klein-Gordon equations *Commun. Pure Appl. Math.* **41** 747–74
- [31] Haller G and Wiggins S 1995 Multi-pulse jumping orbits and homoclinic trees in a modal truncation of the damped-forced nonlinear Schrödinger equation *Physica D* **85** 311–47
- [32] Haller G 1999 *Chaos Near Resonance (Applied Mathematical Sciences vol 138)* (New York: Springer)
- [33] Hărăguș M and Kapitula T 2008 On the spectra of periodic waves for infinite-dimensional Hamiltonian systems *Physica D* **237** 2649–71
- [34] Hasegawa A 1972 Theory and computer experiment on self-trapping instability of plasma cyclotron waves *Phys. Fluids* **15** 870–81
- [35] Jackson R K and Weinstein M I 2004 Geometric analysis of bifurcation and symmetry breaking in a Gross-Pitaevskii equation *J. Stat. Phys.* **116** 881–905
- [36] Jones C K R T 1988 An instability mechanism for radially symmetric standing waves of a nonlinear Schrödinger equation *J. Diff. Eqns* **71** 34–62
- [37] Kapitula T, Kevrekidis P G and Sandstede B 2004 Counting eigenvalues via the Krein signature in infinite-dimensional Hamiltonian systems *Physica D* **195** 263–82
- [38] Kovacic G and Wiggins S 1992 Orbits homoclinic to resonances, with an application to chaos in a model of the forced and damped sine-Gordon equation *Physica D* **57** 185–225
- [39] Lerman L M and Umanskii I A L 1994 Classification of four dimensional integrable Hamiltonian systems and Poisson actions of  $r^2$  in extended neighborhood of simple singular points: I *Russ. Acad. Sci. Sb. Math.* **77** 511–42
- [40] Lerman L M and Umanskii I A L 1994 Classification of four dimensional integrable Hamiltonian systems and Poisson actions of  $r^2$  in extended neighborhood of simple singular points: II *Russ. Acad. Sci. Sb. Math.* **78** 479–506
- [41] Magnus W and Winkler S 1966 *Hill's Equation* (New York: Dover)
- [42] Ma Y C and Ablowitz M J 1981 The periodic cubic Schrödinger equation *Stud. Appl. Math.* **65** 113–58
- [43] McLaughlin D W and Shatah J 1998 Homoclinic orbits for PDE's *Recent Advances in Partial Differential Equations* vol 54 (Providence, RI: American Mathematical Society) pp 281–99
- [44] Menyuk C R 1993 Soliton robustness in optical fibers *J. Opt. Soc. Am. B* **10** 1585–91
- [45] Moloney J and Newell A 2004 *Nonlinear Optics* (Boulder, CO: Westview Press, Advanced Book Program)
- [46] Neishtadt A I and Vasiliev A A 1999 Change of the adiabatic invariant at a separatrix in a volume-preserving 3d system *Nonlinearity* **12** 303–20
- [47] Neishtadt A 1984 The separation of motions in systems with rapidly rotating phase *Prikl. Mat. Mekh. USSR* **48** 133–9
- [48] Radnović M and Rom-Kedar V 2008 Foliations of isoenergy surfaces and singularities of curves *Regular Chaotic Dyn.* **13** 645–68
- [49] Rom-Kedar V 1997 Parabolic resonances and instabilities *Chaos* **7** 148–58
- [50] Rom-Kedar V and Turaev D 2010 The symmetric parabolic resonance *Nonlinearity* **23** 1325–51
- [51] Shlizerman E and Rom-Kedar V 2005 Hierarchy of bifurcations in the truncated and forced nonlinear Schrödinger model *Chaos* **15** 1–22
- [52] Shlizerman E and Rom-Kedar V 2006 Three types of chaos in the forced nonlinear Schrödinger equation *Phys. Rev. Lett.* **96** 024104

- [53] Shlizerman E and Rom-Kedar V 2009 Parabolic resonance: a route to Hamiltonian spatiotemporal chaos *Phys. Rev. Lett.* **102** 033901
- [54] Smale S 1970 Topology and mechanics: I *Invent. Math.* **10** 305–31
- [55] Sulem C and Sulem P-L 1999 Self-focusing and wave collapse *The Nonlinear Schrödinger Equation (Applied Mathematical Sciences vol 139)* (New York: Springer)
- [56] Tennyson J L, John R Cary and Escande D F 1986 Change of the adiabatic invariant due to separatrix crossing *Phys. Rev. Lett.* **56** 2117–20
- [57] Weinstein M I 1985 Modulational stability of ground states of nonlinear Schrödinger equations *SIAM J. Math. Anal.* **16** 472–91
- [58] Zemlyanaya E V and Barashenkov I V 2004 Traveling solitons in the damped-driven nonlinear Schrödinger equation *SIAM J. Appl. Math.* **64** 800–18